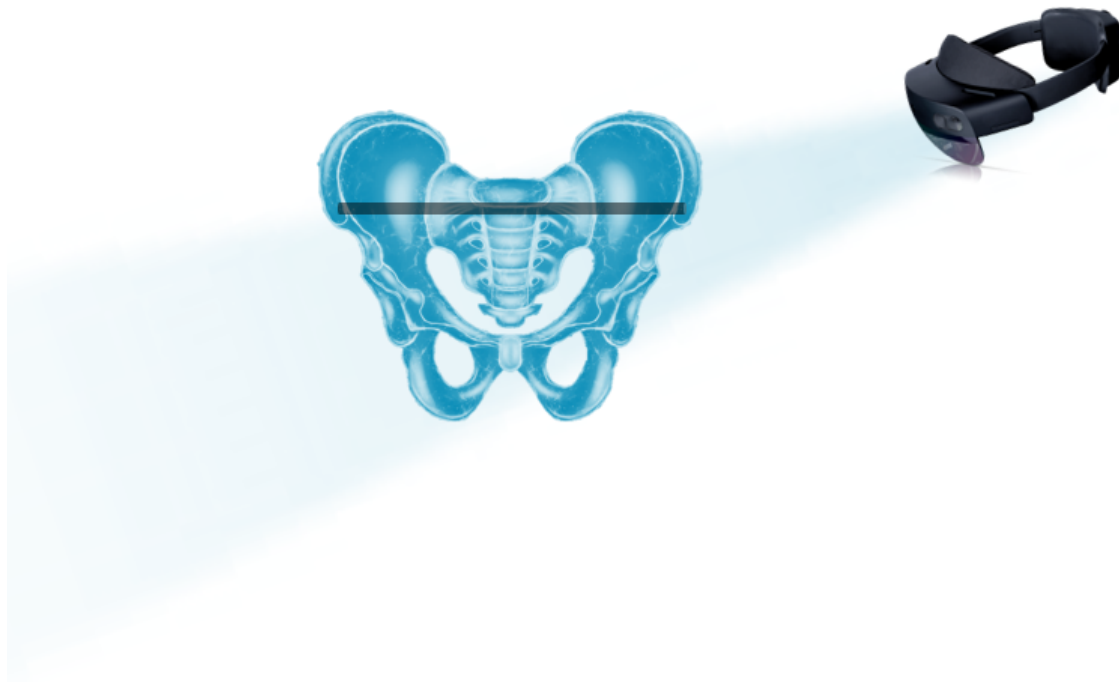


Surgical navigation for traumatic interventions using augmented reality with infrared marker tracking

A proof of concept



A.P. Wang

Technical Medicine, Medical Imaging & Interventions, University of Twente
Department of Trauma Surgery & 3D Lab, Radboudumc Nijmegen

June 6th, 2023

Supervisors:

Prof.dr.ir. C.H. Slump
Dr. V.M.A. Stirlor
Prof.dr. T.J.J. Maal
J.M.J. Duits BSc.
E.M. Walter MSc.
ir. A.G. de Groot

Chairman & Technical supervisor, University of Twente
Medical supervisor, department of trauma surgery, Radboudumc
Technical supervisor, 3D Lab, Radboudumc
Technical supervisor, 3D Lab, Radboudumc
Process supervisor, University of Twente
External member, University of Twente

Abstract

Introduction Percutaneous screw fixation of the pelvis is a difficult procedure with risks of neurovascular damage. The corridors are narrow and an error of a maximum of 2 mm is permitted. In the Radboudumc this procedure is often executed with the 3D-navigation system of Brainlab. The most significant disadvantage of this system is the constant switching between the surgical field and the computer monitors, which increases the cognitive load for the surgeon. To attack this problem, a new surgical navigation technique using augmented reality with infrared marker tracking is introduced.

Methods A reference star and phantom were designed and 3D printed to attach the infrared markers. An algorithm to detect infrared markers with the HoloLens 2 was developed and an augmented reality application was built for a simulated surgical procedure. The aim of the simulation was to place five K-wires into 5 rings with the guidance of the augmented reality application. Five participants performed the experiment. One participant did the experiment 3 times. The placed and planned K-wires were analyzed. Hit/no hit, Δ Euclidean distance of entry point and endpoint, and the angle were evaluated.

Results The phantom was 3D printed and the maximum error of the virtual and physical measurements combined was 0.43 mm. The prototype of the augmented reality application was successfully developed. The IR marker tracking accuracy was 1.44 ± 0.33 mm. The results of the experiment were as follows: 69% of the placed K-wires went through the rings, the mean error of the Δ entry point was 2.57 mm, the mean error of the Δ endpoint was 4.71 mm, and the mean error of the angle was 4.68 mm. For the Δ endpoint and angle, data of the no hits were not included and considered outliers.

Conclusion This study provides a proof of concept for performing percutaneous screw fixation of the pelvis using augmented reality with IR marker tracking as guidance. A simplification of the procedure was performed. Further research is needed to improve the accuracy of the AR application. This can be done by improving the segmentation, registration, and calibration of the augmented reality application. On top of that, adding tool tracking to the augmented reality application should also increase the accuracy. More research is needed to further improve the phantom and the experiment before this surgical navigation technique can be implemented clinically.

Keywords Surgical navigation, augmented reality, infrared markers, percutaneous screw fixation, 3D printing

Contents

1	General introduction	6
1.1	Clinical background	6
1.1.1	Anatomy of the pelvis	6
1.1.2	Pathology of the pelvis	6
1.1.3	Surgical Treatment	7
1.1.4	Percutaneous screw fixation techniques	8
1.1.5	Navigation and imaging techniques for percutaneous screw fixation	8
1.2	Technical background	9
1.2.1	Virtual Reality vs. Augmented Reality vs. Mixed Reality	9
1.2.2	HoloLens 2	10
1.2.3	Depth camera	10
1.2.4	Registration techniques	11
1.3	Research aim	12
1.4	Outline of thesis	12
2	Reference star & phantom	13
2.1	Introduction	13
2.2	Methods	13
2.2.1	Design reference star	13
2.2.2	Design phantom	14
2.2.3	3D printing phantom	15
2.2.4	Gelatin	17
2.2.5	Validation	17
2.3	Results	17
2.4	Discussion	19
2.4.1	Interpretation of the results	19
2.4.2	Limitations	20
2.5	Conclusion	20
3	Augmented reality application for HoloLens 2	21
3.1	Introduction	21
3.2	Methods	21
3.2.1	Access to depth camera	22
3.2.2	Retrieve data	22
3.2.3	Segmentation of IR markers	23
3.2.4	3D position in world coordinates	23
3.2.5	Holographic display	23
3.3	Results	24
3.4	Discussion	25
3.4.1	Interpretation of the results	25
3.4.2	Future research	25
3.5	Conclusion	25
4	Experiment: inserting K-wires	26
4.1	Introduction	26
4.2	Methods	26
4.2.1	Materials	26
4.2.2	Virtual planning	27
4.2.3	AR projection	27
4.2.4	K-wires placement	28
4.2.5	CBCT scanner	28
4.2.6	Segmentation	29

4.2.7	Measurements	29
4.3	Results	30
4.4	Discussion	32
4.4.1	Interpretation of the results	32
4.4.2	Limitations	32
4.5	Conclusion	33
5	General discussion and conclusion	34
	Appendix	38
A	Failed 3D prints	38
B	Segmentation with scattering	39
C	3D reconstructions of the placed K-wires	40

Abbreviations

2D	Two-dimensional
3D	Three-dimensional
APC	Anterior Posterior Compression
AR	Augmented Reality
CBCT	Cone Beam Computed Tomography
CT	Computed Tomography
DICOM	Digital Imaging and Communications in Medicine
FPS	Frames per second
IR	Infrared
kVp	Kilovoltage peak
K-wire	Kirschner wire
LC	Lateral Compression
mA	Miliampere
MR	Mixed Reality
MRI	Magnetic Resonance Imaging
OBJ file	Wavefront 3D object file
OR	Operating Room
ORIF	Open Reduction and Internal Fixation
PLA	polylactic acid
PVA	Polyvinyl alcohol
RGB	Red, Green, Blue
S1	First sacral vertebrae
S2	Second sacral vertebrae
STL	Standard Triangle Language
ToF	Time-of-Flight
VLC	Visible light camera
VR	Virtual Reality
VS	Vertical Shear

1 General introduction

1.1 Clinical background

1.1.1 Anatomy of the pelvis

The pelvis consists of two large hip bones, called the os coxae. These include the ilium, ischium, and pubis bones, see figure 1. These three parts connect at the acetabulum. Anteriorly, the two os coxae are joined by the pubic symphysis. Posteriorly, the os coxae are attached to each side of the sacrum, creating the sacroiliac joint.[1] The stability of the pelvic ring depends on the ligamentous structures.[2] The pubis and ischium connect with each other inferiorly, creating an opening called the obturator foramen. The obturator nerve, vein and artery pass through this foramen to exit the pelvic cavity. The main function of the pelvic bones is to diffuse the weight of the upper body onto the lower limbs and to protect the organs that lie within the pelvic cavity.[1]

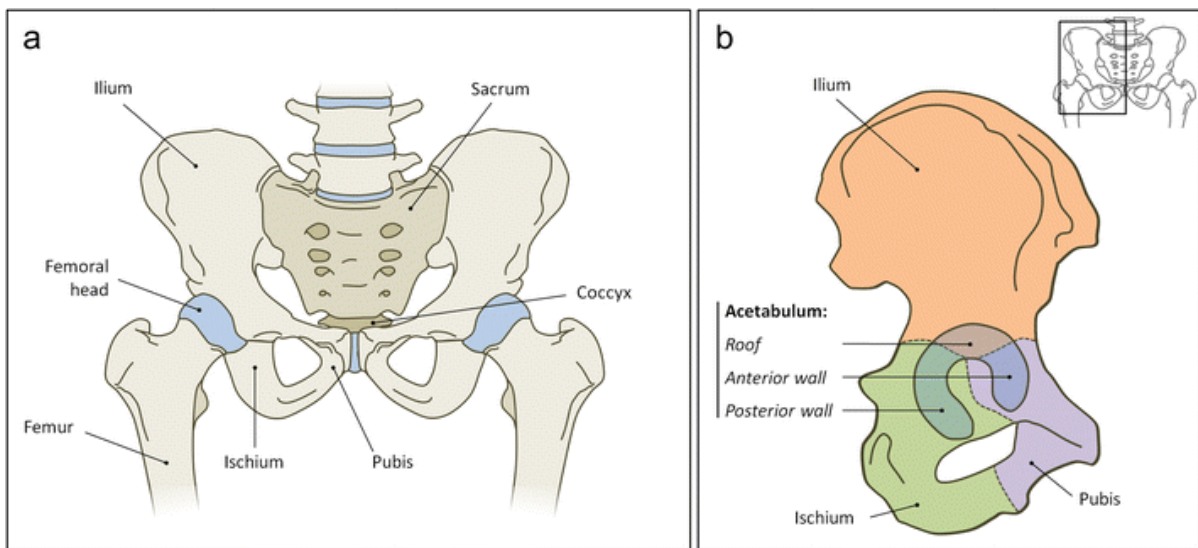


Figure 1: Anatomy of the pelvis. **a** Ventral view of the pelvic region with cartilaginous parts in blue. **b** Lateral view of the right hemipelvis. The ilium (orange), ischium (green) and pubis (purple) all contribute to the acetabulum (blue)[3]

1.1.2 Pathology of the pelvis

Pelvic injuries are often caused by a high-energy traumatic event and are associated with significant morbidity and mortality.[2], [4] Pelvic injuries are seen in 3 – 10% of all trauma patients.[4]–[7] There are three types of pelvic fractures: acetabular fractures, sacral fractures and pelvic ring fractures. For pelvic ring fractures, displacement can only occur if there is a fracture in at least two locations.[2] A commonly used classification for pelvic ring injuries is the Young-Burgess Classification.[8] This classification is based on the direction and location of the applied force, as well as the injury pattern. The trauma mechanism is divided into three groups: Anterior Posterior Compression (APC), Lateral Compression (LC) and Vertical Shear (VS), see figure 2.[9] Treatment decision is based on the pelvis stability, fracture displacement, associated injuries and the patient’s physiological status.[8], [10] In general APC type I and LC type I are stable injuries with minimal displacement, which can often be treated conservatively. Ligamentous injuries and fractures such as VS and APC/LC types II and III often need surgical intervention, as these injuries create instability of the pelvis.[2], [8]

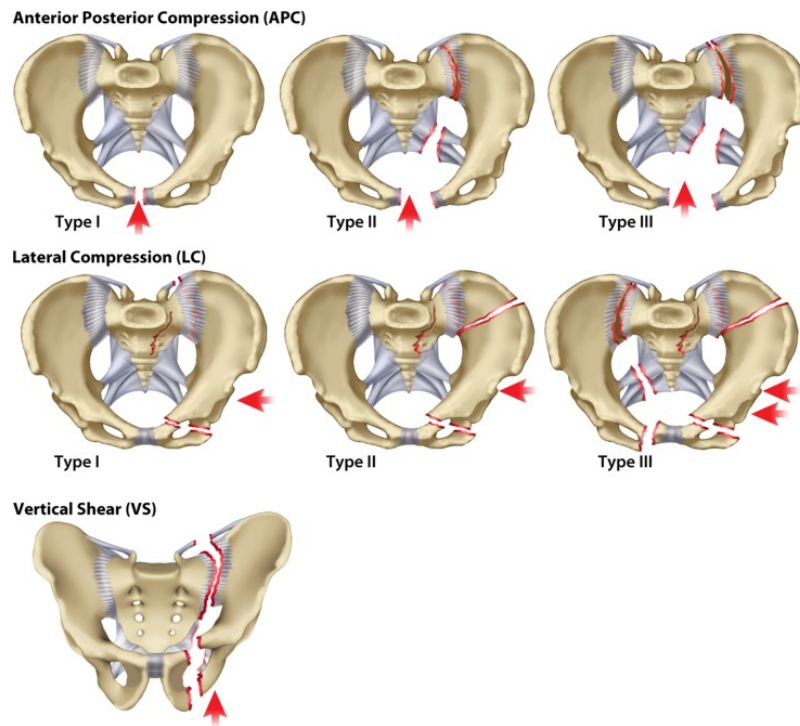


Figure 2: Young-Burgess Classification [9]

1.1.3 Surgical Treatment

There are three types of surgical treatment for pelvic injuries: external fixation (figure 3a), open reduction and internal fixation (ORIF), (figure 3b) and closed reduction with percutaneous fixation (figure 3c). External fixation is often used for stabilization in the acute setting when the patient is hemodynamically unstable, but it can also be used as a definitive treatment. This method is effective in rotationally unstable injuries with displacement. However, for unstable rotational and vertical injuries combined, ORIF provides better fracture reduction and biomechanical stability than external fixation. With this technique plates and screws are placed to stabilize the fracture. Pelvic ring fractures can also be treated with percutaneous screw fixation. This method is preferred over open surgical fixation because it is less invasive, has minimal blood loss, a shorter surgical time and gives adequate stability.[6], [11]

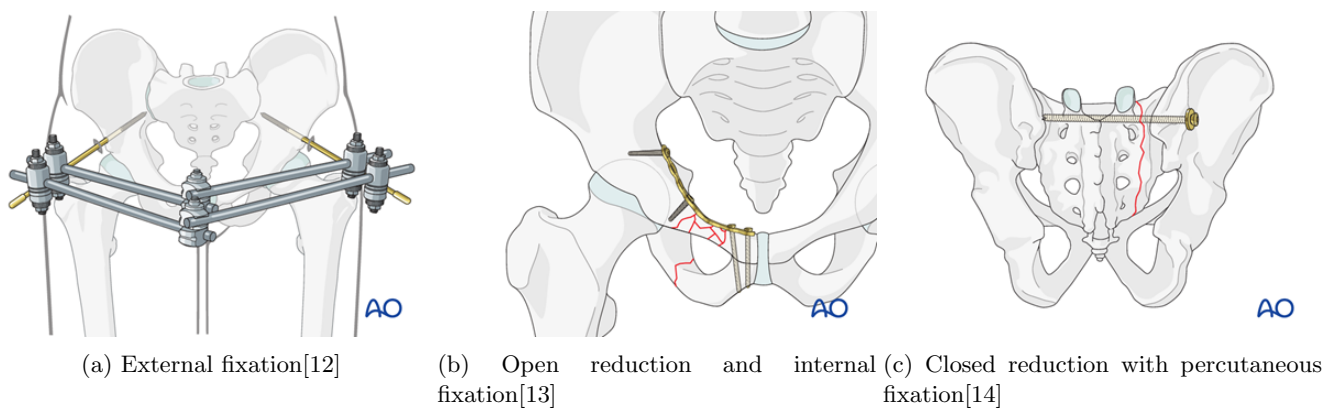


Figure 3: Surgical treatments for pelvic injuries

1.1.4 Percutaneous screw fixation techniques

There are a few types of screws that can be used in percutaneous screw fixation for the pelvic bone, see figure 4. For sacroiliac fixation, a trans-sacral screw (red) or an ilio-sacral screw (yellow) can be placed to give the posterior ring stability. Other screws that can be placed percutaneously are the posterior (blue) and anterior (green) column screws for acetabular fractures.[11] The positioning of the screws is technically challenging. The insertion point, direction and angle of the screw need to be established for correct positioning.[11] Literature describes that a deviation of four degrees may cause the screws to go through the foramen of the first sacral vertebrae (S1) or even the anterior wall of the sacrum.[15] Wagner et al.[16] assessed the dimensions of trans-sacral corridors in three-dimensional (3D), measuring a mean cranio-caudal diameter of 11.6 ± 5.4 mm and an anterior-posterior diameter 23.2 ± 5.7 mm for the S1 corridor and a cranio-caudal diameter 14.0 ± 2.4 mm and an anterior-posterior diameter 17.6 ± 2.3 mm for the second sacral vertebrae (S2) corridor. Caviglia et al.[11] assessed the anterior and posterior column corridors. The anterior column corridor narrows first in the middle of the pubic ramus with a mediolateral diameter of 20.2 ± 4.1 mm and a superior-inferior diameter of 15.9 ± 2.4 mm. The second narrowing section is located at the center of the acetabulum with a mediolateral diameter of 38.2 ± 4.1 mm and a superior-inferior diameter of 15.1 ± 1.8 mm. The narrow area of the posterior column corridor is approximately 6.1 mm. The ilio-sacral screws often have a diameter of 6.5 or 7.3 mm. Resulting in a margin of a maximum between 2.15 and 2.55 mm from the screw to the edge of the bone. As this can differentiate between each patient and depending on which diameter screw is used, an accuracy of a minimum of 2 mm was aimed in this study.

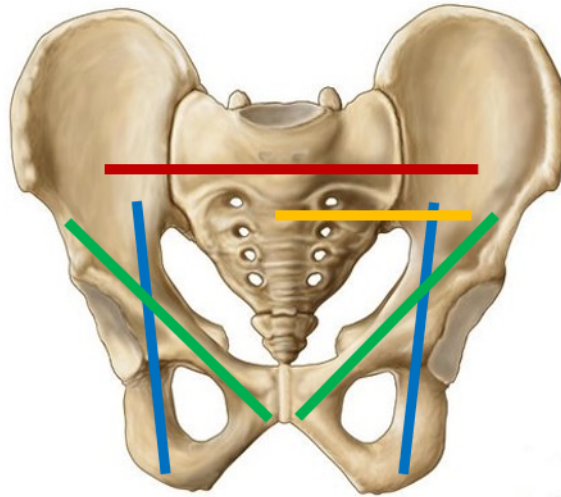


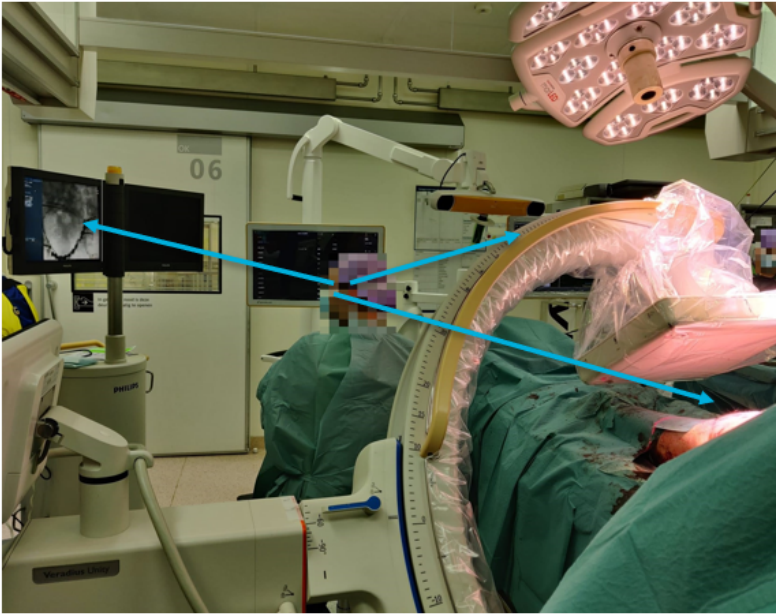
Figure 4: Screw pathways in the pelvic bone. In red: trans-sacral screw, yellow: ilio-sacral screw, green: anterior column screws, blue: posterior column screws.

1.1.5 Navigation and imaging techniques for percutaneous screw fixation

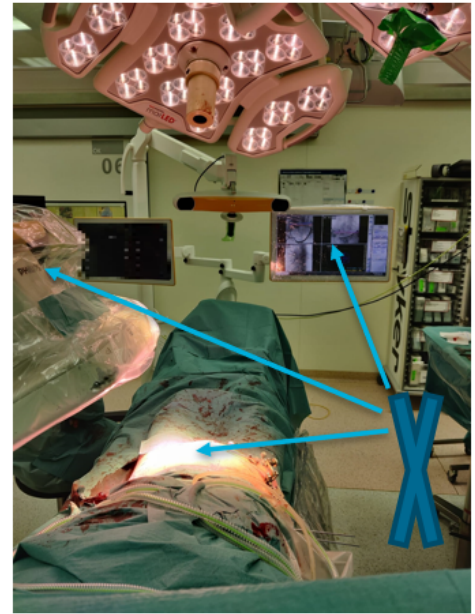
In order to perform percutaneous screw fixation of the pelvis, guidance of a navigation or imaging technique is needed. First, the percutaneous approach can be performed with fluoroscopic guidance. With fluoroscopy, an X-ray image of the patient can be made. The challenges of fluoroscopy are that it only creates two-dimensional (2D) images which makes the assessment of the pelvis difficult. The surgeon needs to translate these images to a 3D patient.[17] On top of that, creating a good image of the pelvis can be challenging and the frequent changes between the inlet, outlet, anterior/posterior and lateral view are time-consuming. This leads to high radiation exposure for the patient as well as for the staff.[11], [18]

The introduction of 3D navigation techniques is to increase the accuracy of screw placement and decrease radiation exposure. [11], [18], [19] Complications such as bleeding and nerve damage due to a misplaced screw may be prevented.[6], [20], [21] At the Radboud university medical center (Radboudumc), a level-

one trauma center in the Netherlands, the use of a 3D-navigation system (Brainlab curve, Brainlab, Germany) for placing SI screws is the gold standard. The system shows how to position the K-wire on a computer monitor and gives feedback about the position and direction of the K-wire to the surgeon. When the position of the K-wire is within the 2 mm range, the surgeon drills the K-wire into the patient. However, this system has some disadvantages like the initial learning curve of the system and the prolonged operation time caused by the registration. Furthermore, constantly having to switch between the surgical field and the computer monitors may also cause errors. The setup of the Brainlab system in the operating room (OR) can be seen in figure 5. The surgeon located at X needs to look in three different directions: two screens while operating on the patient.[17], [22], [23]



(a) View 1 in OR, the doctor's assistant needs to look in three different directions (blue arrows) during the surgery.



(b) View 2 in OR, the surgeon is seated at the place of X, operating on the patient while looking at the screen at the end of the bed and checking the screw placement on the second screen (blue arrows)

Figure 5: Brainlab setting in the OR, where the Brainlab system is positioned at the end of the bed and the X-ray scanner on the left side of the patient.

To overcome the disadvantages of this 3D navigation technique, a new method with augmented reality (AR) is investigated. With AR techniques the positioning of screws for minimally displaced fractures can be planned preoperatively and visualized intraoperatively. Just like 3D navigation, using the AR technique may result in smaller incisions, better screw positioning, fewer complications, reduced operation time, less radiation exposure[24] and a better clinical outcome. However, the biggest advantage of the AR technique is that the surgical planning can be projected on the surgical field which eliminates having to switch focus between a computer monitor and the surgical field.[22], [23] This will decrease the cognitive load of the surgeon, possibly resulting in better focus and preventing any errors during surgery.[23]

1.2 Technical background

1.2.1 Virtual Reality vs. Augmented Reality vs. Mixed Reality

The differences between virtual reality, augmented reality and mixed reality will be discussed below. Virtual reality (VR) is a technology that simulates a virtual 3D environment where the user can explore and interact with the virtual world via wearable headsets.[25] Augmented reality (AR) works in a similar way as VR, but the difference is that it can superimpose virtual objects onto the real-world environment.[25] AR may be used for training in educational settings, planning and surgical navigation. Because of the growing demand for visual feedback in the OR, AR-based navigation systems

were developed.[26] These systems can be applied to visualize 3D images from CT or MRI data and to superimpose these 3D reconstructions onto the patient in the field of view of the surgeon.[26], [27] This way the preoperative scans can be combined with the intraoperative setting, creating real-time information and surgical guidance for the surgeons. AR technology has been applied in various fields of surgery such as neurosurgery, orthopedic and spine surgery, laparoscopic surgery and oral surgery.[26] Mixed Reality (MR) is often confused with AR. MR allows the user to interact with both the virtual and the real world.[28] While in AR, objects do not interact with the real world, but are only superimposed onto a real object. In this thesis, an AR application is developed where a hologram is superimposed onto an object.

1.2.2 HoloLens 2

As mentioned above, in AR a wearable headset is used to superimpose virtual objects onto the real-world environment. A wearable headset that often is used for AR is the HoloLens 2 from Microsoft (Microsoft Corporation, Redmond, WA, USA). This headset contains 4 visible light environment tracking cameras (VLC), 1 RGB camera and 1 depth camera (figure 6). With the cross-platform game engine Unity (version 2021.3.5f1, Unity Technologies, San Francisco, USA), an AR application could be developed and built for the HoloLens 2.

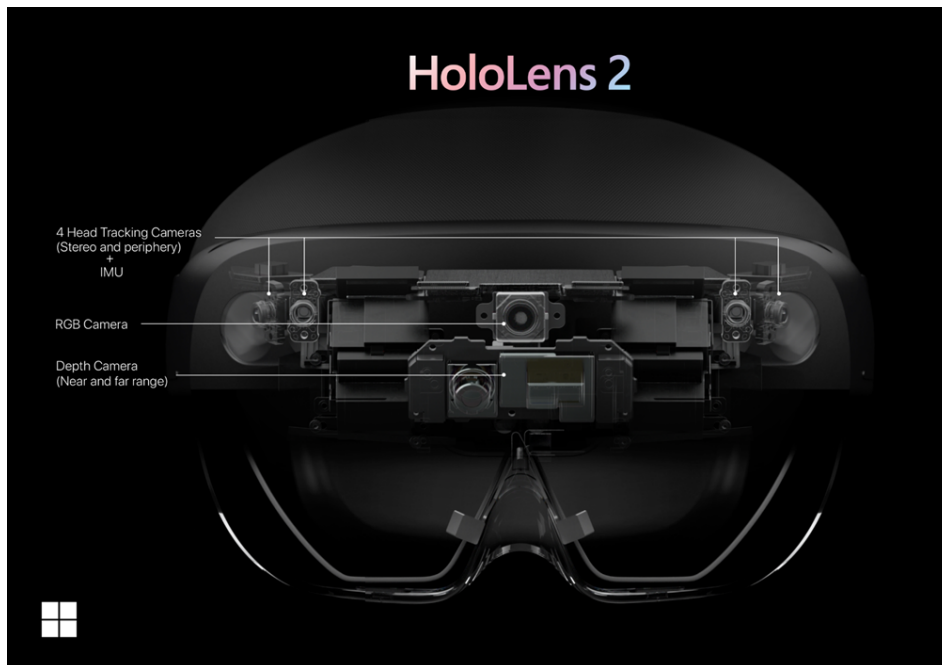


Figure 6: Cameras on the HoloLens 2.[29]

1.2.3 Depth camera

For this research, the Time-of-Flight (ToF) depth sensor will be used to track infrared (IR) markers. The basic principle is as follows: The ToF system contains a light source that emits near-infrared light, that will be reflected by the object. A sensor that is sensitive to this wavelength will capture the reflected light and it measures the time between emitting and receiving the light.[30] The distance can be estimated with the following formula:

$$d = \frac{c\Delta T}{2} \quad (1)$$

with d the distance, c the speed of light and ΔT the time between emitting and receiving the light. The depth sensor has two modes: a short throw and a long throw mode. The short mode has a high frequency of maximal 45 frames per second (FPS) and is used to track the hand of the user, while the long throw mode has a low frequency of 1-5 FPS and is used to map the environment.[31], [32] The images all have a size of 512x512 pixels, but only the pixels within the circle contain values as depicted in figure 7.[31] For both modes a depth and a reflectivity image are created (figure 8).

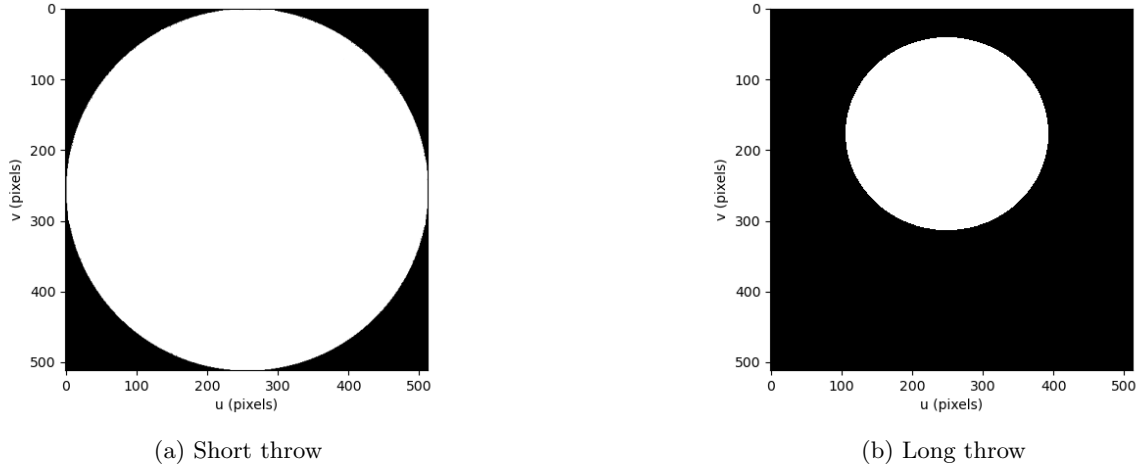


Figure 7: In white are the pixels containing values for short throw (a) & long throw mode (b).

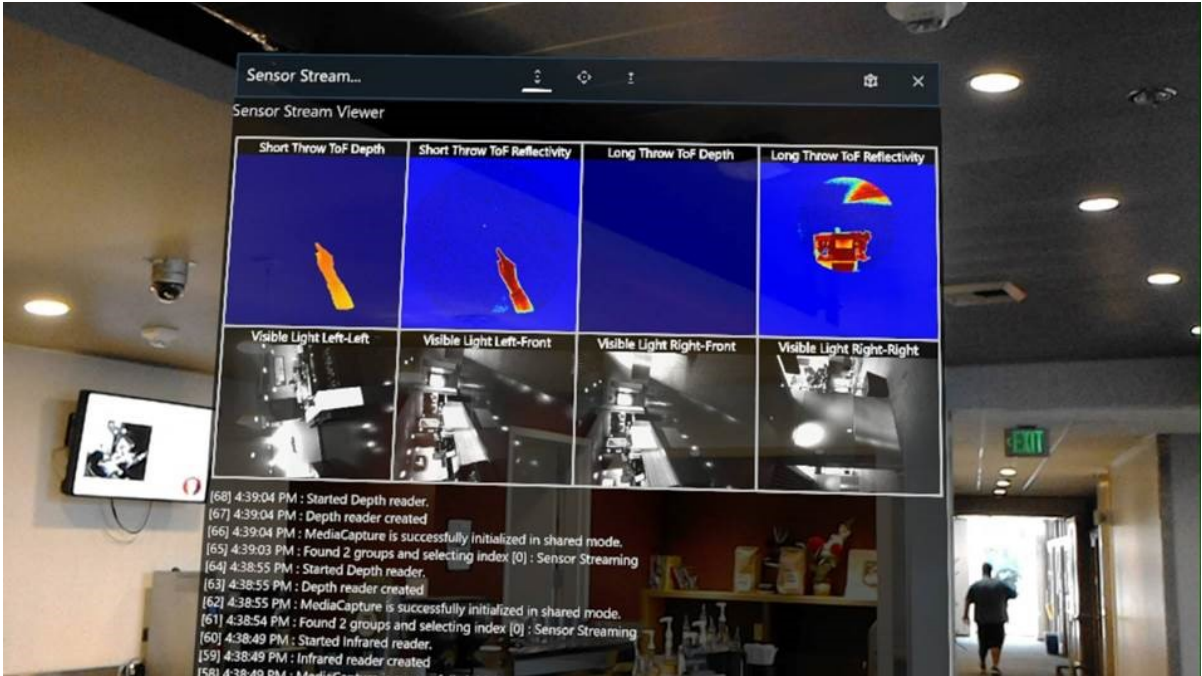


Figure 8: A mixed reality capture of a test application that displays the eight sensor streams available in Research Mode.[32]

1.2.4 Registration techniques

There are several registration techniques to superimpose holograms onto a patient. Marker-based tracking is a commonly used technology for these kinds of applications. Two-dimensional markers in the form of a QR code already exist, such as AprilTags (figure 9a), Aruco and Vuforia.[27] However, the biggest disadvantage of these markers is that the accuracy and precision are not high and steady enough for the clinical procedure. In this study, the strive is to have an accuracy of a minimum of 2 mm. Cao et al.[33] researched the registration accuracy with different registration methods including Vuforia. The best result was an accuracy of 2 mm at a distance of 46.1 cm from the marker. However, at a distance of 54.1 cm from the marker the accuracy drops down to 1.3 cm. Another study showed an accuracy of 2.3 mm with a maximum error of 3.5 mm.[34] These kinds of deviations are not acceptable for percutaneous screw fixation of the pelvis. Other methods like markerless registration use surface or contour matching of anatomical landmarks. However, for percutaneous screw fixation, this is often not possible because of the surgical drape that is covering the patient.[27] Kunz et al.[27] investigated two different approaches for

tracking 3D IR markers (figure 9b) with the HoloLens. One method was to use the short throw reflectivity and short throw depth from the near field ToF sensor. This approach had a tracking accuracy of 0.76 mm at a distance of 40-60 cm. In this thesis, a similar registration technique with IR markers is investigated for the HoloLens 2.

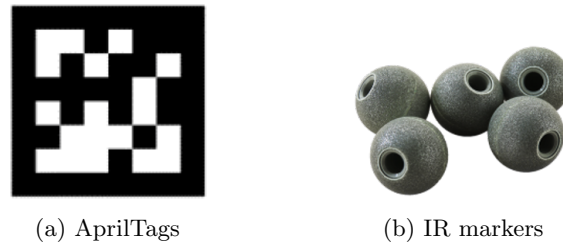


Figure 9: Example of 2D (a) and 3D (b) markers

1.3 Research aim

Interest in a new surgical navigation technique is present among surgeons. It is important to have accurate screw positioning in percutaneous screw fixation of pelvic fractures because of the narrow corridors that can cause neurovascular damage. In Radboudumc the gold standard for placing SI screws is the use of a 3D navigation system. However, the biggest disadvantage is the constant switching between the surgical field and the computer monitors. This increases the cognitive load of the surgeon which may cause errors. Augmented reality may solve this problem by using holographic images of the patient and superimposing them on the patient. In order to display the holograph correctly on the patient, IR markers will be used instead of 2D markers because of the big inaccuracies. The primary aim of this thesis is to provide a proof of concept for using augmented reality with infrared marker tracking on the HoloLens 2 as a surgical navigation technique. In order to analyze the accuracy of the developed augmented reality application, a phantom with a reference star is designed and printed in 3D. These will then be used for an experiment where a simulation of the procedure will be performed. During this experiment, five K-wires will be placed inside the phantom with the guidance of the AR application. The differences between the planned and placed K-wires will be compared. The second aim of this thesis is to investigate the accuracy of the developed augmented reality application while performing a simulation of the clinical procedure.

1.4 Outline of thesis

This thesis is divided into several chapters. In **Chapter 2**, the design and the 3D printing of the reference star and the phantom for the experiment will be explained. Virtual and physical validation of the phantom was performed and compared with the design. **Chapter 3** contains the development of the algorithm to track IR markers and the augmented reality application to superimpose the hologram onto the phantom. **Chapter 4** describes the experiment where K-wires will be placed with the guidance of the AR application. The accuracy & precision of the placed K-wires will be analyzed. Finally, in **Chapter 5**, a general discussion, recommendations and conclusion were given.

2 Reference star & phantom

2.1 Introduction

For the augmented reality application, a novel registration technique with multiple IR markers will be used. In order to keep the IR markers in their fixed position, a reference star is designed and 3D-printed. The reference star will be attached to the phantom. A phantom will be created for the experiment where a simplified simulation of the percutaneous screw fixation will be executed. This experiment will be further explained in Chapter 4. The aim of this chapter was to elaborate on the design and the 3D-printing process of the reference star and the phantom. Validation of the 3D printed phantom will be performed where the virtual and physical measurements were compared with the design. The results are used to determine whether the planning for the experiment can be made based on the design.

2.2 Methods

For the design of the reference star and the phantom, the 3D computer graphics program Autodesk 3ds Max 2023 (Autodesk Media and Entertainment, San Rafael, CA, USA) was used. The design is reviewed for any errors in Autodesk Netfabb (Autodesk Media and Entertainment, San Rafael, CA, USA). For 3D printing, the software Ultimaker Cura 5.1.1 was used as a slicing application for 3D printers. The design is then 3D printed using the Ultimaker S5 (Ultimaker, Utrecht, The Netherlands).

2.2.1 Design reference star

The first step was to design a reference star to attach the IR markers to. This star can also be used to attach to the phantom. The design is based on the first star of previous research conducted at the 3D-lab of the Radboudumc[34] (figure 10). This star had three arms with on each arm three places where the IR marker can be fixated. The walls around the three holes are higher so that the screw head can fit into the gap. At the center of the star, a mount is attached.

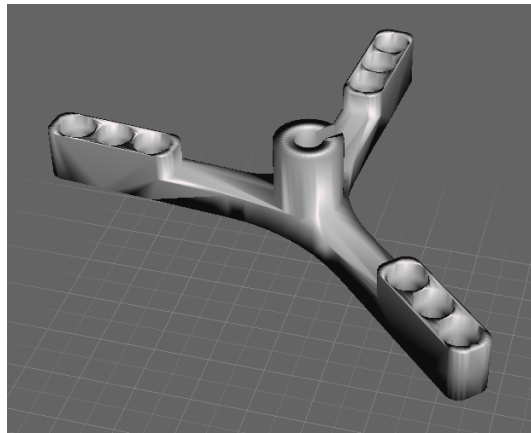


Figure 10: Original reference star

The first adjustment was to make a reference star with four arms with different angles in between so more data on the IR markers could be generated. In addition, this creates an asymmetrical shape that can be used to determine the orientation of the reference star (figure 11a). The second adjustment was to create the four arms with different lengths so the distances to the center would vary. The different arms length can be distinguished from each other which can be used to determine the orientation of the reference star even better. The attachment in the center was not used and therefore it was removed (figure 11b). The third version was a star with arms at different angles in all three axes (figure 11c). The hypothesis was that extra information could be retrieved from the third dimension and therefore lead to a better result. However, due to the time restrictions of this thesis, it has been decided to limit the number of parameters and keep the design simple. For the fourth version, an extra hole at the center was created for a fifth IR marker (figure 11d). This creates an extra data point and connection to the rest of the markers. After attaching reference star 4 to the phantom, it was noticed that the walls at the end of each arm were

difficult to 3D print. Therefore, a last version was created without these walls (figure 11e). All reference stars except star 3 were printed with polylactic acid (PLA) pearl white, while reference star 3 was printed with PLA blue. All stars were printed with print core AA 0.4. The fifth star was only 3D printed in combination with the phantom with PLA red.

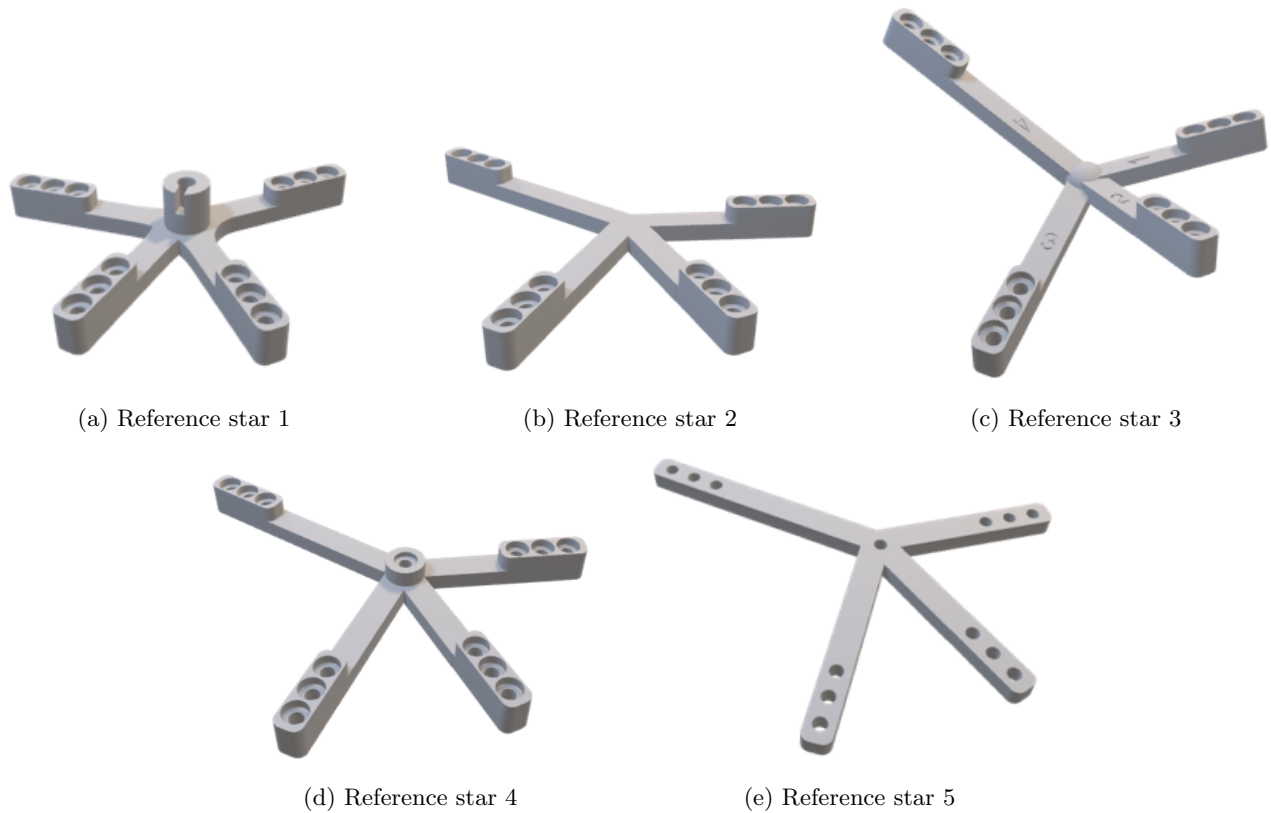


Figure 11: Reference stars 1-5 in order of development

2.2.2 Design phantom

For the experiment, a phantom was designed. The concept was to simulate percutaneous screw fixation in a simplified phantom. Several ideas were sketched (figure 12). The design for options A and B were target based. However, the clinical procedure is not focused on hitting a target such as tumor ablation. The relevant characteristics of the simulation are that the screw needs to stay in its path and not breach the corridors of the pelvis. Therefore, option C was designed where the cylinders simulate the corridors of a pelvis. However, the risk of this design was that the cylinder may be guiding the screw in the right direction. To overcome this problem option D was created where the cylinders are simplified into rings. The rings could be seen as the cortex of a bone where the screw needs to go through the center.

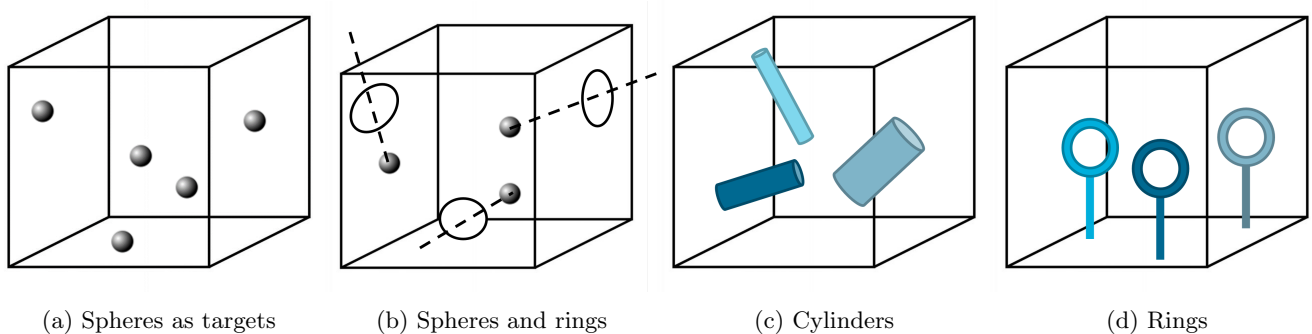


Figure 12: Sketches for the phantom

With the concept of the rings, the first version of the phantom was designed (figure 13a). The phantom had a size of $225 \times 120 \times 150$ mm and contains five different rings as targets. The front plane was at a 45° angle and had five holes which were the insertion sites for the screws. Again, it was decided to keep the phantom as simple as possible, to eliminate multiple variables that could influence the results. Therefore in the second version, all rings had equal size and orientation with an inner diameter of 12 mm, an outer diameter of 20 mm and an angle at 45° . The inner diameter of 12 mm was chosen, because this is the smallest diameter of the S1 corridor.[16] Attached to this phantom was the fourth version of the reference star (figure 13b). However, this phantom was too large to fit into the Cone Beam Computed Tomography (CBCT) scanner (KaVo OP 3D Vision, Biberach an der Riss, Germany). Therefore, the size was adjusted to $150 \times 80 \times 100$ mm. The intention was to fill the phantom with gelatin in order to keep the screws in place after insertion. For this concept, an extendable front plane was created so it could be switched with a plane without holes in it. However, this construction led to leakage while filling the phantom. To overcome this problem, a third version was made where the phantom is a rectangle box with on top a lid containing five openings. The rings are oriented parallel to the lid (figure 13c). This version has reference star five attached to it. An extra support was added to the rings, to make sure that the phantom could be 3D printed.

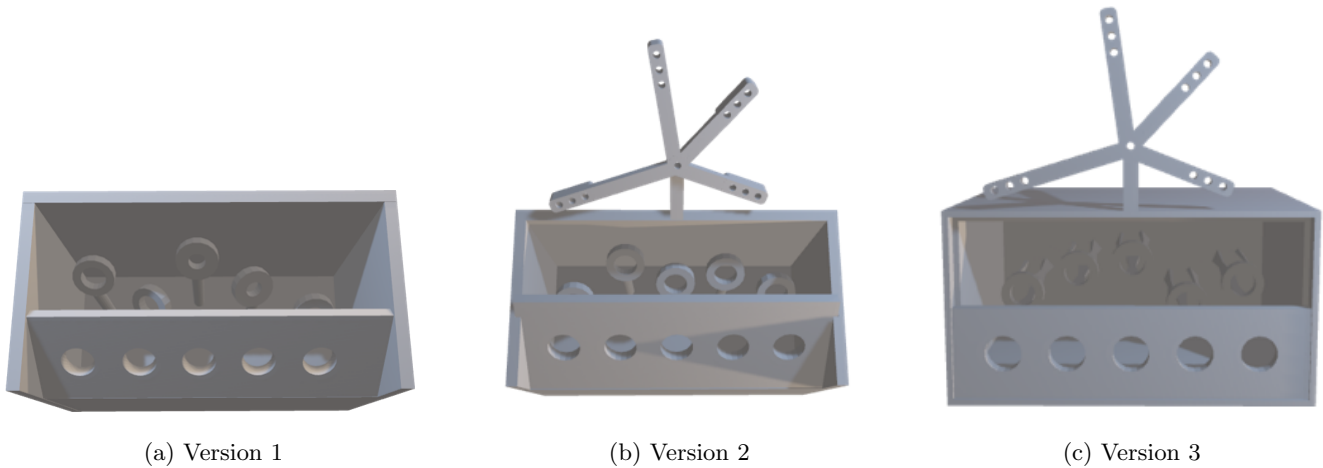


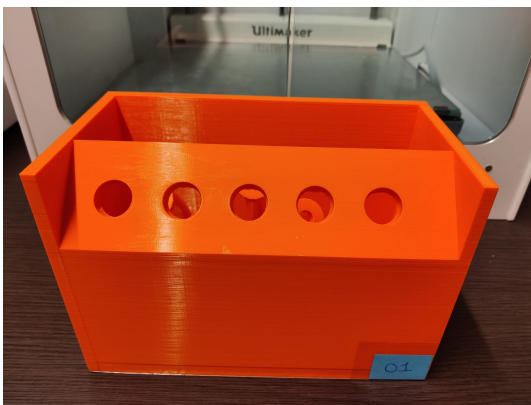
Figure 13: Three versions of phantoms in order of development

2.2.3 3D printing phantom

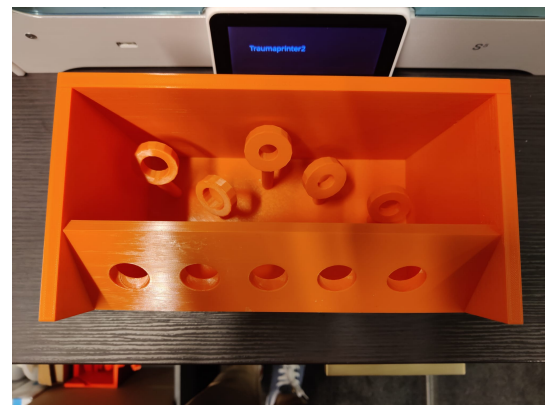
There were multiple prints made from the three versions that were described previously. Not all prints were successfully 3D printed due to human errors or errors of the 3D printer. The print settings from nine phantoms can be found in table 1. Other settings that are not mentioned were all on default. The combination of these settings mostly depended on available materials and time. Most of the phantoms were printed with PLA Red, because this material was well visualized by CT.[35] Phantom 7 was a version where the objects needed support to be printed successfully. However, printing the support with the same material (PLA Red) made it very difficult to remove the support, causing the objects to break. An alternative was to print the support with polyvinyl alcohol (PVA) natural. This material is water-soluble and convenient to use as support. Despite this knowledge, after two attempts using this material, no prints were successfully finished (see Appendix A). In figure 14 the printed phantoms that corresponds to the three designed versions can be seen.

Phantom	Material	Printcore	Infill
Phantom 1	PLA Orange	AA 0.4	20%
Phantom 2	PLA Red	AA 0.4	60%
Phantom 3	PLA Red	AA 0.4	70%
Phantom 4	PLA Red	AA 0.4	70%
Phantom 5	PLA Red	AA 0.8	70%
Phantom 6	PLA Red	AA 0.8	70%
Phantom 7	PLA Red & PVA natural	AA 0.8, BB 0.8	100%
Phantom 8	PLA Red	AA 0.4	30%
Phantom 9	PLA Blue	AA 0.8	30%

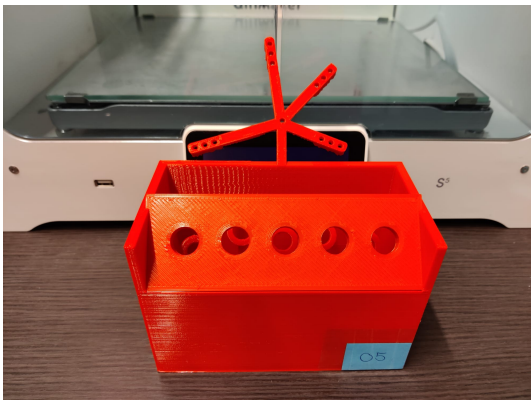
Table 1: Print settings



(a) Phantom 1, front view



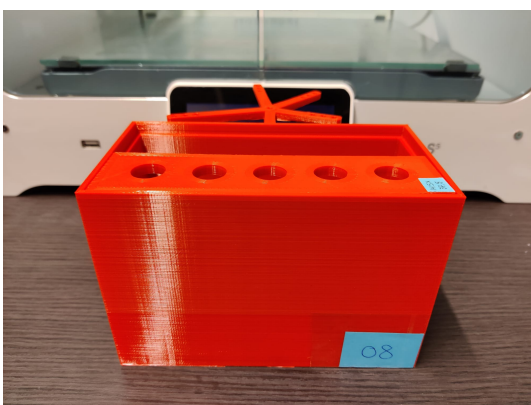
(b) Phantom 1, top view



(c) Phantom 5, front view



(d) Phantom 5, top view



(e) Phantom 8, front view



(f) Phantom 8, top view

Figure 14: Three versions phantoms printed in 3D

2.2.4 Gelatin

For the experiment, instruments will be inserted into the phantom. In order to keep these instruments in place after insertion, the phantom was filled with gelatin. The advantage of gelatin is that it is liquid during the filling, but hardens over time. In addition, gelatin was easy to remove so the phantom could be reused. The gelatin mixture was made with 20 grams of gelatin dissolved in 850 mL water. Red food coloring was added to make the rings less visible. The phantom was placed in the refrigerator overnight to become solid.

2.2.5 Validation

A comparison was made in order to validate if the printed phantom was similar to the designed version. This was realized by measuring the printed phantom physically and virtually. For the physical measurement, a digital caliper was used. For the virtual measurement, the phantom was scanned with the CBCT scanner. The scan protocol of the UHD model scan was used with the following settings: volume size of 23 cm diameter \times 17 cm height, voxel size of 0.3 mm, scan time of 17.8 seconds, exposure time of 7.4 seconds, with 120 kVp and 5 mA. The phantom was positioned at an angle while scanning to avoid scattering. The Digital Imaging and Communications in Medicine (DICOM) files were loaded in the medical image processing software Materialise Mimics (version 24.0, Materialise NV, Leuven, Belgium) to create a 3D reconstruction and saved as a Standard Triangle Language (STL) file. The STL file was then loaded in 3DMedX (version 1.2.29.3, Radboudumc, Nijmegen, The Netherlands) to conduct the virtual measurements. The physical and virtual measurements were executed by the same three participants. Each participant did one physical measurement and three virtual measurements. In total 13 distances were evaluated, the distances between each of the IR markers (A-E), as well as the length, width and height of the phantom (figure 15).

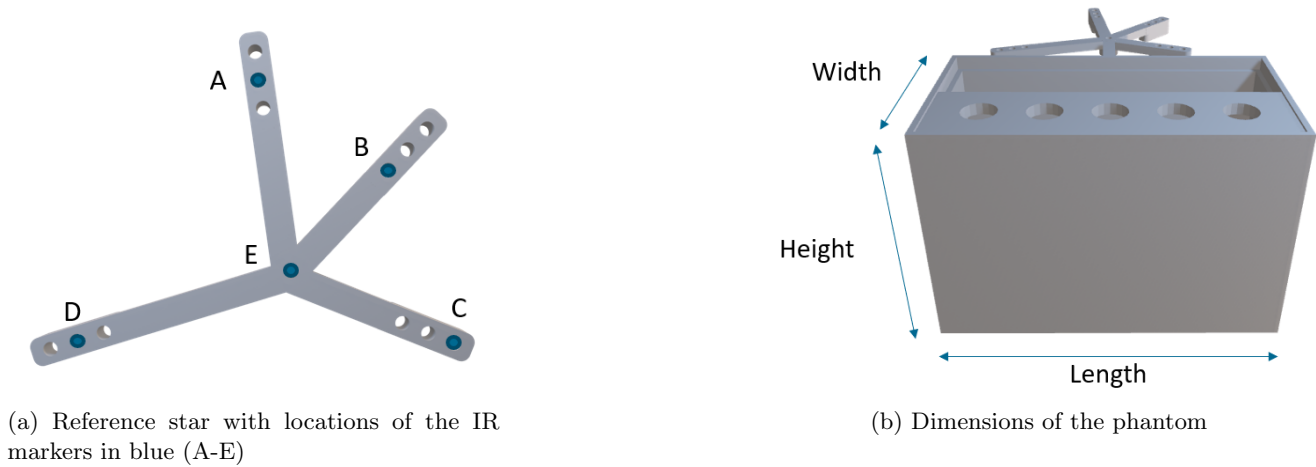


Figure 15: Parameters for the validation

2.3 Results

In figure 16 the 3D reconstruction of the phantom after segmentation can be seen. Table 2 presents the design values and the results of the physical and virtual measurements. These measurements were then compared to the design values. A distance map was created after repositioning the 3D reconstructed phantom with the designed phantom, see figure 17. The colormap at the bottom of the figures ranges from -5 mm (red) to +5 mm (green).

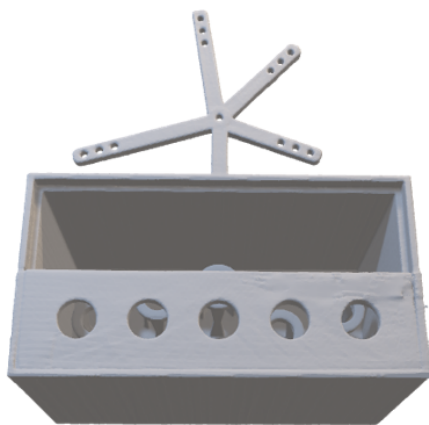


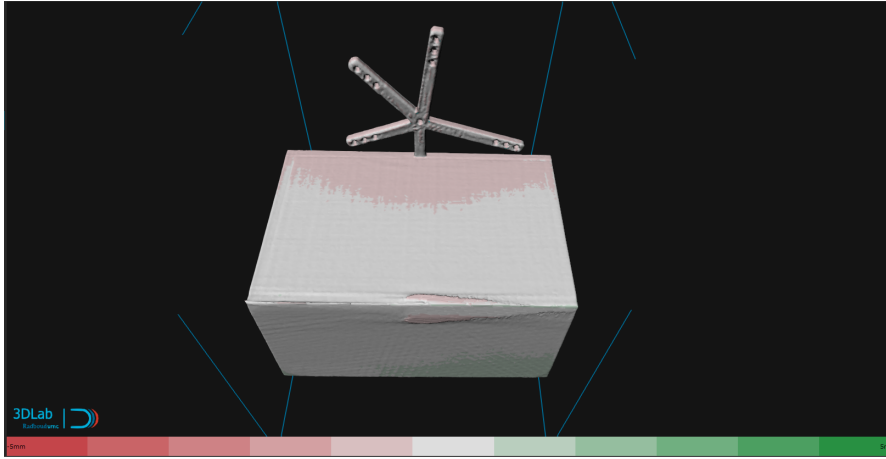
Figure 16: 3D reconstruction of phantom 8

Table 2: The virtual and physical measurements (mm) of the phantom compared to the design

mm	Design	Virtual Mean \pm SD	Physical Mean \pm SD	Virtual-Design	Physical-Design	Mean error
AE	42.79	42.66 \pm 0.17	42.77 \pm 0.18	-0.13	-0.02	-0.08
BE	31.00	30.97 \pm 0.13	31.47 \pm 0.36	-0.03	0.47	0.22
CE	39.64	39.60 \pm 0.21	39.63 \pm 0.23	-0.04	-0.01	-0.03
DE	50.16	49.78 \pm 0.20	50.17 \pm 0.05	-0.38	0.01	-0.19
AB	34.68	34.59 \pm 0.22	34.57 \pm 0.30	-0.09	-0.11	-0.10
BC	41.23	41.20 \pm 0.18	41.12 \pm 0.22	-0.03	-0.11	-0.07
CD	83.94	83.55 \pm 0.22	83.91 \pm 0.12	-0.39	-0.03	-0.21
DA	70.59	70.11 \pm 0.23	70.78 \pm 0.04	-0.48	0.19	-0.14
AC	72.62	72.58 \pm 0.26	72.40 \pm 0.23	-0.04	-0.22	-0.13
BD	78.75	78.40 \pm 0.22	78.89 \pm 0.08	-0.35	0.14	-0.11
Width	80	79.59 \pm 0.45	80.14 \pm 0.09	-0.41	0.14	-0.13
Length	150	149.01 \pm 0.38	150.13 \pm 0.10	-0.99	0.13	-0.43
Height	100	99.17 \pm 0.54	100.00 \pm 0.07	-0.83	0.00	-0.42



(a) Front view, the distance map of phantom 8



(b) Back view, the distance map of phantom 8

Figure 17: Distance map between 3D reconstructed and designed phantom 8 with a colormap from -5 mm (red) to +5 mm (green).

2.4 Discussion

2.4.1 Interpretation of the results

Table 2 shows the measured distances between the markers and the width, length and height of the phantom. It can be seen that the differences between the virtual measurements and the design values are all under 0.5 mm except for the length and height of the phantom. There are multiple causes that could lead to these errors. There could be inaccuracies in the 3D printing, inaccuracies in the scanning of the phantom by the CBCT scanner, or inaccuracies during the segmentation. Additionally, the method of virtual measurement could also cause errors. The participants had to select two points at each end to measure the distance in a straight line. This method is subjective as it depends on the assessment of the participant and whether the line was straight. To overcome this problem, an objective assessment could be done by calculating the distances automatically and repeatedly. Another finding is that the values of the virtual measurements were all smaller than the design. This can be clarified by the selected points for the measurements. These points are selected on the mesh and can not be placed outside of it. This results in a distance equal to or smaller than the design. In addition to the virtual measurements, the phantom was also measured physically. The difference between the physical measurements and the design was all under 0.5 mm. The maximum error of the virtual and physical measurements combined is 0.43 mm. This shows an error under 0.5 mm between the printed phantom and the design.

As shown in figure 17, an overlay between the designed phantom and the 3D reconstructed phantom was created. A distance map was then plotted to see the differences. It can be seen that the 3D reconstructed phantom matches correctly with the design in general. In figure 17a it can be noticed that the biggest deviation is located at the lid. The lid is a separate object that is placed on top of the phantom without fixation. This creates a space between the phantom and the lid making small movement possible. In figure 17b some deviation can be seen at the upper back of the phantom in red and at the bottom in green. This can be clarified by the matching of the 3D reconstructed phantom and its design which needed a little bit more rotation to the front. The deviation in red at the bottom of the phantom is caused by the support underneath the phantom which was needed during the scan in the CBCT-scanner. The border between the phantom and the support was difficult to segment. This caused some irregularities in the 3D reconstruction.

For the experiment, it was decided to eliminate the extra steps of scanning and segmenting the phantom. Instead, the design and its planning were used as objects for the AR application. The conclusion was made that the print error of 0.43 was neglectable. However, it is good to realize that the error may have some effect on the planning that can cause systematic errors. This could influence the results of the analyses done in Chapter 4.

2.4.2 Limitations

In this research, only the angle and the distances between the IR markers were taken into account. It was designed so that each IR marker had a unique position with different distances to the center. Additionally, the angles between the two IR markers were different in order to create a reference star without symmetry. However, no research has been done to establish the ideal shape of a reference star. An improved shape of the reference star may ensure better accuracy for the detection of the IR markers by the HoloLens 2. Additionally, further research should be conducted about the ideal number of IR markers that need to be used. Cao et al. compared the registration accuracy with the number of markers (AprilTags)[33]. Similar research could be done for the IR markers where the trade-off between the number of IR markers and the size of the design must be made.

Gelatin was used for the filling of the phantom. In order to reuse the phantom, the gelatin was removed and replaced with new gelatin. In order to remove the gelatin, warm water was used to make the gelatin liquid again and a spoon was used to scoop the gelatin out. This removal was not without risks. The glass transition temperature of PLA is around 60°C.[36] Therefore, an accidental collision could modify the rings. To overcome this problem, investigation of other materials that do not require replacement or high temperature for the removal should be considered.

After the first time scanning phantom 8, a lot of scattering was present at the bottom and top of the phantom during segmentation (see Appendix B). The artifacts were very hard to remove from the phantom. This scattering could be explained by the grazing of the X-ray beams against the flat surfaces on the top and bottom of the phantom. The scanner rotates horizontally, so this problem was not present for the other surfaces. Knowing this, the phantom was positioned at an angle during scanning. Another possible solution could be changing the phantom's design.

A simplified phantom was made for the experiment. However, the next steps will be performing experiments on a more realistic phantom that is similar to the anatomy of the pelvic bone. In a previous study[37], an anthropomorphic model of the pelvis has been created which had similar anatomical and radiological characteristics as tissue. However, more research is needed to produce a 1:1 scale model. Other possibilities could be using sawbones or cadavers.

2.5 Conclusion

The aim of this chapter was to show the design and 3D-printing process of the reference star and the phantom. Analyses were made to compare the 3D-printed phantom with its design. The differences were small, so the print error was neglected. Further research is needed to create a better reference star and a more anatomically realistic phantom.

3 Augmented reality application for HoloLens 2

3.1 Introduction

Augmented reality can be used as a tool to superimpose anatomy onto the patient in 3D. This enables physicians to look inside the patient. On top of that, it can also be used as a surgical navigation tool. For this latter application, it is necessary to have an accurate overlay. Different types of markers and registration methods are known.[27] Kunz et al. developed a new registration method, using IR markers with the HoloLens. This showed promising results with submillimeter accuracy.[27] For the percutaneous screw fixation of the pelvis, an accuracy of less than 2 mm is needed. Further investigation is essential to determine its potential. Therefore in this study, an algorithm was developed to detect IR markers with the HoloLens 2. The aim of this chapter is to describe the development of the algorithm to track IR markers. In addition, a custom-made Augmented Reality application was built for the experiment that will be described in Chapter 4.

3.2 Methods

The workflow of developing an AR application is as follows (figure 18): IR markers need to be tracked with the depth camera of the HoloLens 2. First, the depth camera needs to be accessed by turning the research mode on. A reflectivity and a depth image are retrieved. Then, the IR markers are segmented and the 2D position is calculated. After normalization the values of the depth image are appended, creating a 3D position in camera coordinates. With a transformation matrix is the 3D position in camera coordinates converted to world coordinates. After this, the design of the reference star and the phantom were used for the holographic display. In order to superimpose the hologram at the right place, an algorithm for registration and calibration was applied.

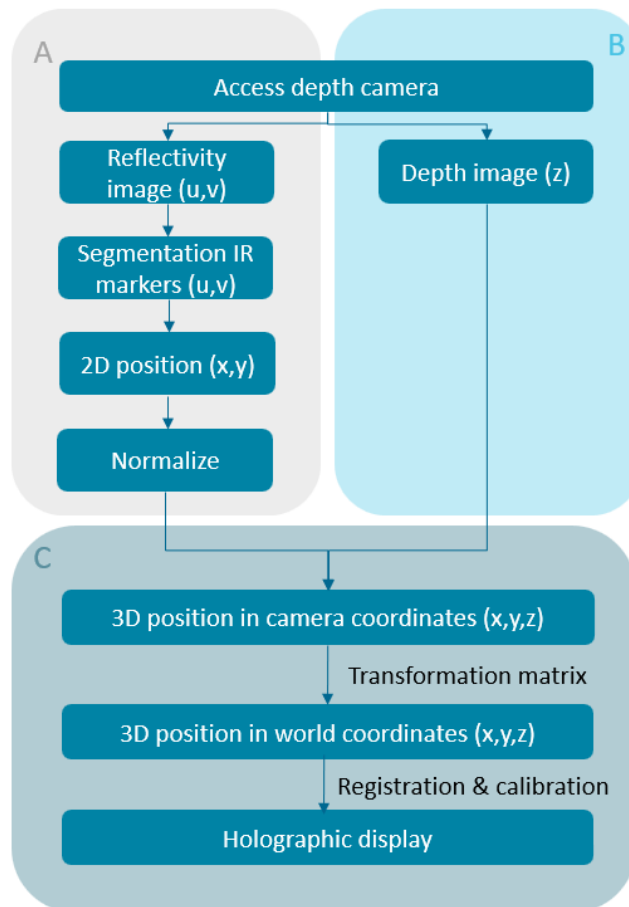


Figure 18: Workflow of the AR application. A:Workflow to get xy coordinates, B:z coordinate, C:IR markers in 3D position (x,y,z).

3.2.1 Access to depth camera

The first step was to gain access to the raw streams of the depth camera from the HoloLens 2. On Github a project was found called HoloLens2ForCV[32] where four sample apps about using research mode streams were available. The research mode of the HoloLens 2 can be turned on which enables access to the camera streams. Furthermore, a second project on GitHub called HoloLens2-ResearchMode-Unity[38] was used. This project contained a Unity Plugin for using research mode functionality in HoloLens 2, which was based on HoloLens2ForCV. After following the steps as described in this project, the depth camera was accessed and the stream was visualized in real-time on the HoloLens 2. In figure 19 a reference star can be seen in the background. At the center are the depth and reflectivity images from the short throw mode of the depth sensor. The two outer images are from the VLCs and will not be used in this research. This also applies to the point cloud reconstruction.

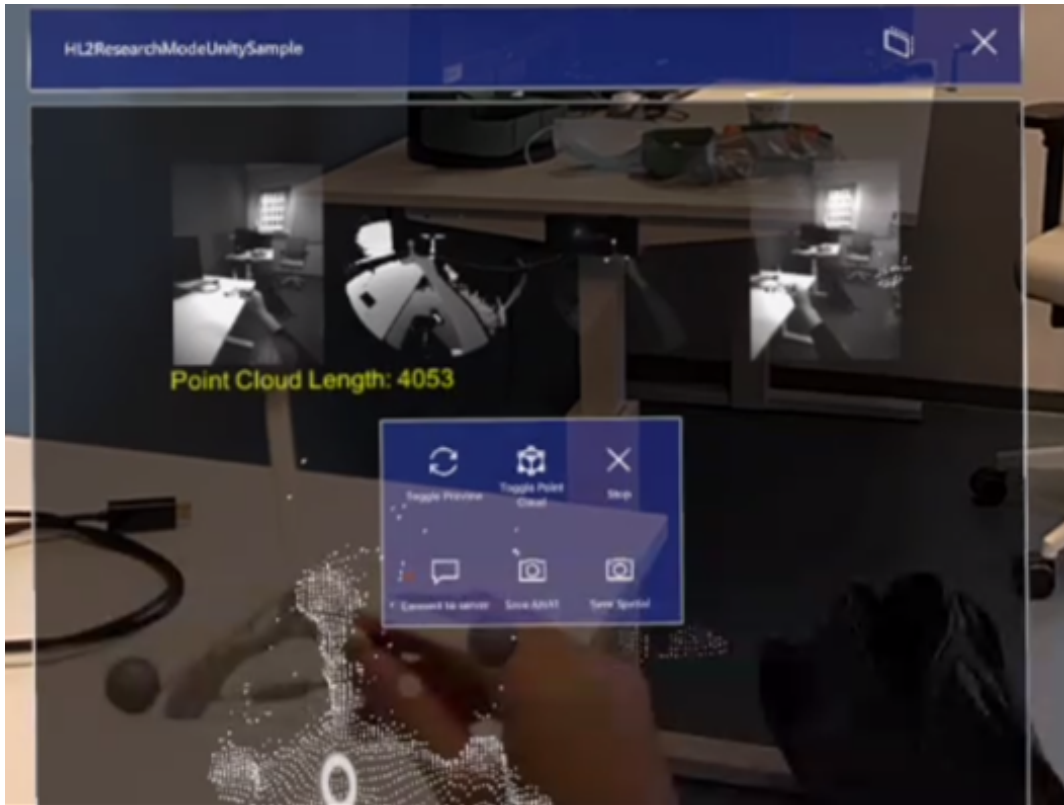


Figure 19: Access streams from the HL2ResearchModeUnitySample. A reference star with three IR markers was held. The short throw stream was on. Four streams can be seen from left to right: left front VLC image, depth image, reflectivity image and right front VLC image. The menu is visible at the center and underneath is the point cloud image pictured.

3.2.2 Retrieve data

The next step was to retrieve the depth and reflectivity data from the HoloLens 2. After reshaping the data, an image of 512×512 pixels can be created as illustrated in figure 20. The depth image can be seen on the left side and the reflectivity on the right side. It is noticeable that the pixels within the circle have values as previously mentioned. On the reflectivity image, the IR markers can be clearly distinguished from the environment.

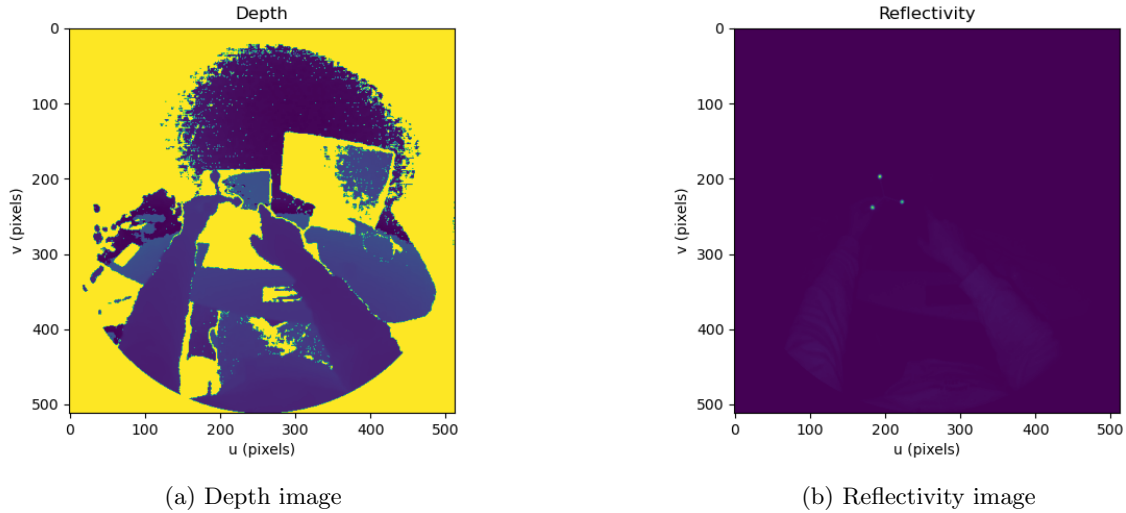


Figure 20: Depth and reflectivity images from short throw mode.

3.2.3 Segmentation of IR markers

The IR markers can be segmented from the reflectivity image. The moving average filter was applied to segment the IR markers. This filter replaces each pixel with the average pixel value of it and a neighborhood window of adjacent pixels which in this case are two pixels in every direction. This creates an average pixel value of 5×5 pixels. After this, a threshold is applied to create a binary image where the IR markers have a value of 1 and the rest of the image a value of 0. The pixel coordinates are then matched to the corresponding IR marker, and the center of each IR marker is calculated. An experiment to investigate the accuracy of the detection of IR markers by the HoloLens 2 was executed. In total ten subjects participated. The subjects needed to face the reference star at six different positions. At each position, the HoloLens 2 took a snapshot and the distances between each of the markers were calculated. The distances were then compared to the distances in the original design.

3.2.4 3D position in world coordinates

The depth and reflectivity images are in polar coordinates (u,v) . In order to get the xy coordinates, (u,v) needed to be converted to Cartesian coordinates (x,y) . The Cartesian coordinates were then normalized. The z -coordinate was retrieved from the depth image and added to the homogeneous coordinates, establishing a 3D position. However, this 3D position is located in the camera coordinate system and needs to be converted into the world coordinate system. This is realized by applying a transformation matrix.

3.2.5 Holographic display

In order to superimpose the virtual models correctly onto the 3D-printed phantoms, registration of the IR markers and calibration of the HoloLens 2 were needed. For the registration, a brute-force Procrustes algorithm was applied to the five IR markers. This algorithm was applied, because it calculates every possibility between the five virtual and real markers. The root mean square error was used to select the correct combination which had the lowest error. In figure 21 the virtual 3D model can be seen in Unity. After loading the AR application onto the HoloLens 2, a hologram is seen with a frame rate of 60 fps. It was noticed that the hologram was displaced to the left of the actual reference star. Therefore calibration was needed to correct for the holographic offset. The hypothesis was that the offset was caused by the depth camera that was positioned more on the left side of the HoloLens 2. Therefore, an offset of 1.5 mm to the right was manually added.

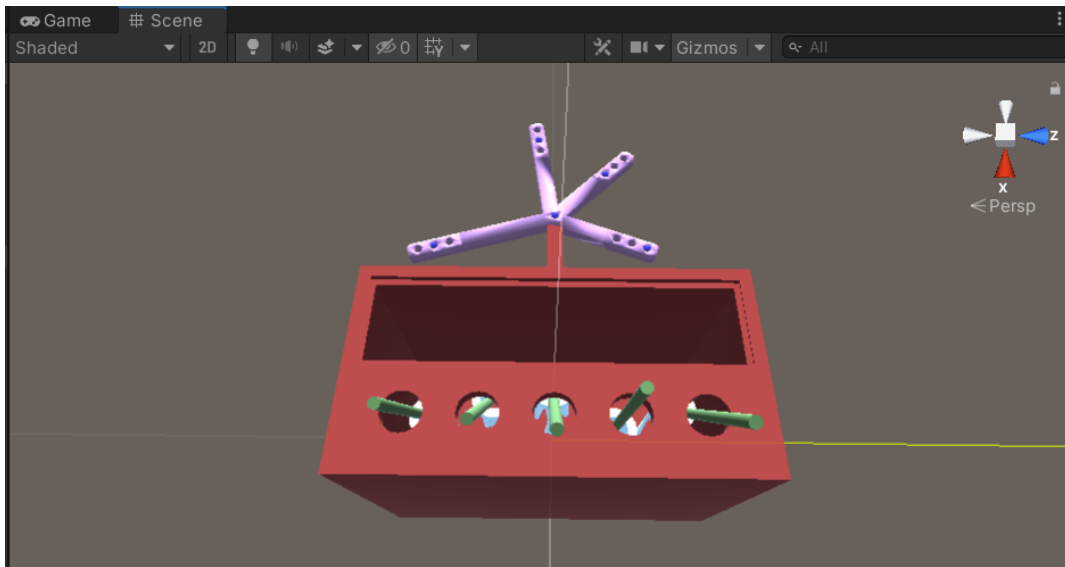


Figure 21: Objects in Unity, with reference star (purple), phantom (red), planned K-wires (green), rings (white).

3.3 Results

In figure 22 the virtual object is superimposed onto the reference star. The blue dots represent the center point of the IR markers that are calculated by the HoloLens 2. The IR marker tracking accuracy was 1.44 mm with a standard deviation of 0.33 mm. The maximum error was 2.63 mm.



Figure 22: Holographic display of the reference star. The center point of the IR markers is shown as blue dots

Figure 23 shows the overlay of the virtual objects onto the real phantom. The virtual objects are the phantom (red), reference star (purple), IR markers (spheres), planning (green) and the rings (not visible).

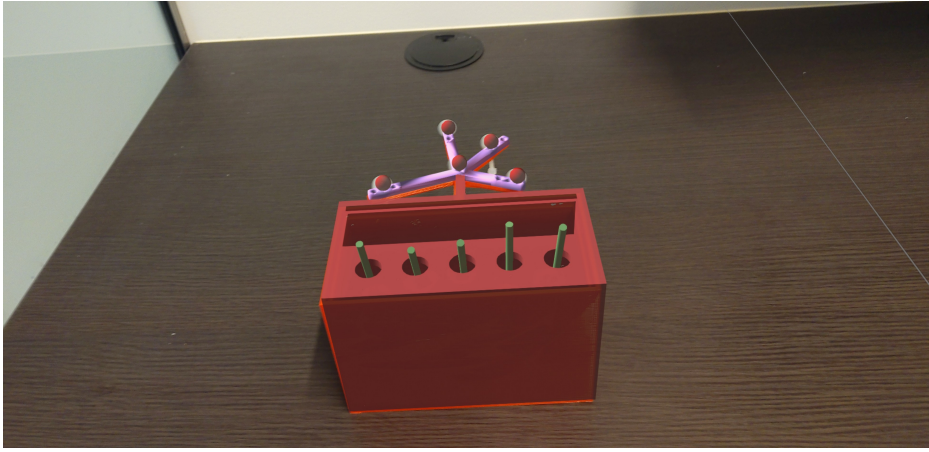


Figure 23: Holographic display of the phantom onto the 3D printed phantom

3.4 Discussion

3.4.1 Interpretation of the results

As can be seen in figure 22, the hologram is successfully superimposed on the reference star. However, the display of the hologram is not always accurate. The displacement can be best seen at the arm on the most right. The hologram is positioned a bit too high compared to the reference star. The IR marker tracking accuracy was 1.44 ± 0.33 mm. This is under the 2 mm that is needed for the procedure. However, the performance of placing screws was not included. This will be investigated in the next chapter. Figure 23 shows the projection of the hologram onto the phantom. Displacement can be seen on the left side of the phantom, the bottom of the phantom and the reference star. This suggests that the virtual phantom needs to be shifted downwards. The first prototype has been developed, but more research is needed to improve the IR marker tracking and the holographic display.

3.4.2 Future research

Further research is needed to reach higher accuracy for IR marker tracking. First, more investigation is needed for the segmentation of the IR markers. Other methods like edge detection[39] (Sobel, Laplacian of Gaussian, Canny edge detection, etc.) or blob detection[27] should be performed and compared. Second, research should be conducted to compare different registration methods. In this study, a brute force algorithm was used for the registration of the markers. This approach tries all possible solutions and finds the best solution. It is applicable in this study because only five IR markers were used. When more IR markers are utilized, this algorithm becomes inefficient and slow.[40] Other options like iterative closest point algorithm[41] or aligning triangles algorithm[33] should be tested. A comparison of the registration time and the registration accuracy could be made. Third, more research is needed to determine if the hologram is placed in the correct position. In this study, eye calibration was not always executed. To ensure the best overlay for each subject, eye calibration should be performed each time. In addition, the holographic shift was manually adjusted by adding an offset of 1.5 mm to the right. An investigation should be performed to map out the offset for different positions of the HoloLens 2. Angles and distances between the HoloLens 2 and the phantom could be analyzed. Cao et al. showed that the offset in the y-direction increases radially out from the origin.

3.5 Conclusion

The first prototype of the AR application with IR marker tracking for the HoloLens 2 has successfully been developed. The results look very promising as the accuracy is under the limit of 2 mm. However, there is still a lot of room for improvement. More research about segmentation, registration and calibration methods should be done. In addition, a simulation of the procedure needs to be executed to see if the accuracy is still sufficient. This will be described in the next chapter.

4 Experiment: inserting K-wires

4.1 Introduction

The clinical goal is to eventually perform percutaneous screw fixation with augmented reality as guidance. This experiment was created as a proof of concept to investigate the possibilities and the potential of using AR for surgical navigation. Previous chapters described the design of the phantom and the development of the application on HoloLens 2. These elements will be used for an experiment, where the planned K-wires are superimposed onto the phantom by the HoloLens 2. A simplified simulation of the clinical procedure was created. In this chapter, the experiment will be elaborated and the accuracy and precision will be analyzed.

4.2 Methods

As shown in figure 24, the workflow of the experiment consists of six steps. First, virtual planning of the K-wires is created and used for the AR projection. With the HoloLens 2, the planning is projected onto the phantom which is used to place the K-wires through the rings. After placement, the phantom will be scanned with the CBCT scanner. From the DICOM files, the phantom and the K-wires will be segmented. The 3D reconstruction and the planning are then used for the analysis. These steps will be elaborated in the next paragraphs.

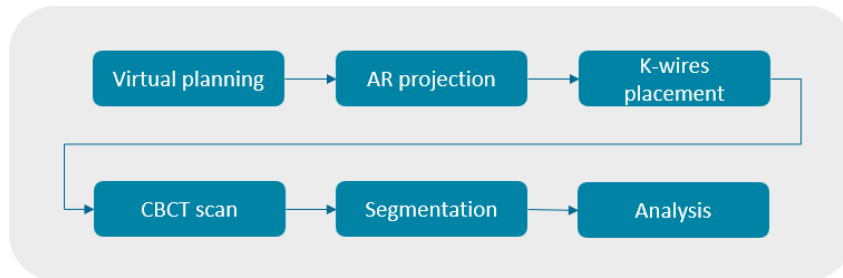


Figure 24: Workflow of the experiment

4.2.1 Materials

For the experiment a HoloLens 2, a phantom filled with gelatin, five IR markers and five K-wires were needed. K-wires were used, because during the clinical procedure a K-wire is placed before the screw is inserted. On top of that it was cheaper and easier to obtain than screws. The K-wires were collected after they had been used for surgery. For the experiment a support of 45 degrees was placed underneath the phantom in order to simulate the position of the patient. In figure 25 the set up of the experiment is illustrated.

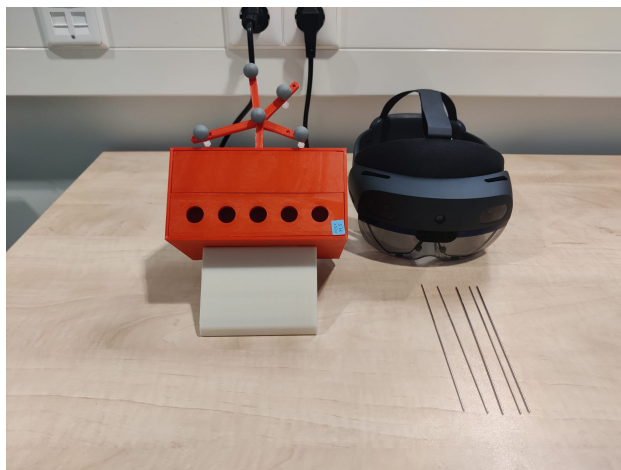


Figure 25: Setup experiment containing the phantom with five IR markers, support, five K-wires and a HoloLens 2

4.2.2 Virtual planning

The first step was to create a virtual planning in Autodesk 3ds Max. The planning was made based on the phantom's design, see figure 26. Five cylinders with a diameter of 4 mm and a length of 12 cm were placed through the center of the opening and the rings. The phantom, rings, reference star, lid with openings and planning were saved separately as a Wavefront 3D object file also called OBJ file.

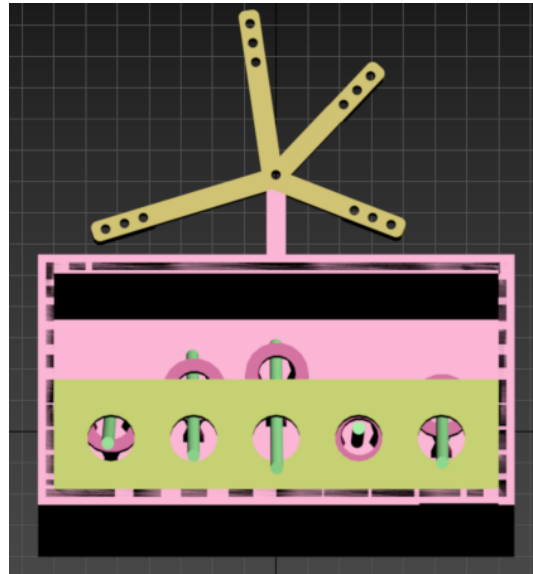


Figure 26: Designed phantom with each part saved separately as an OBJ file. Reference star in yellow, phantom in light pink, rings in dark pink, lid with openings in green and the planned K-wires in green cylinders.

4.2.3 AR projection

The OBJ files were loaded into Unity. A custom application was made for the HoloLens 2. Running the application on the HoloLens 2, a projection of the rings and the planning could be seen on the phantom, see figure 27.

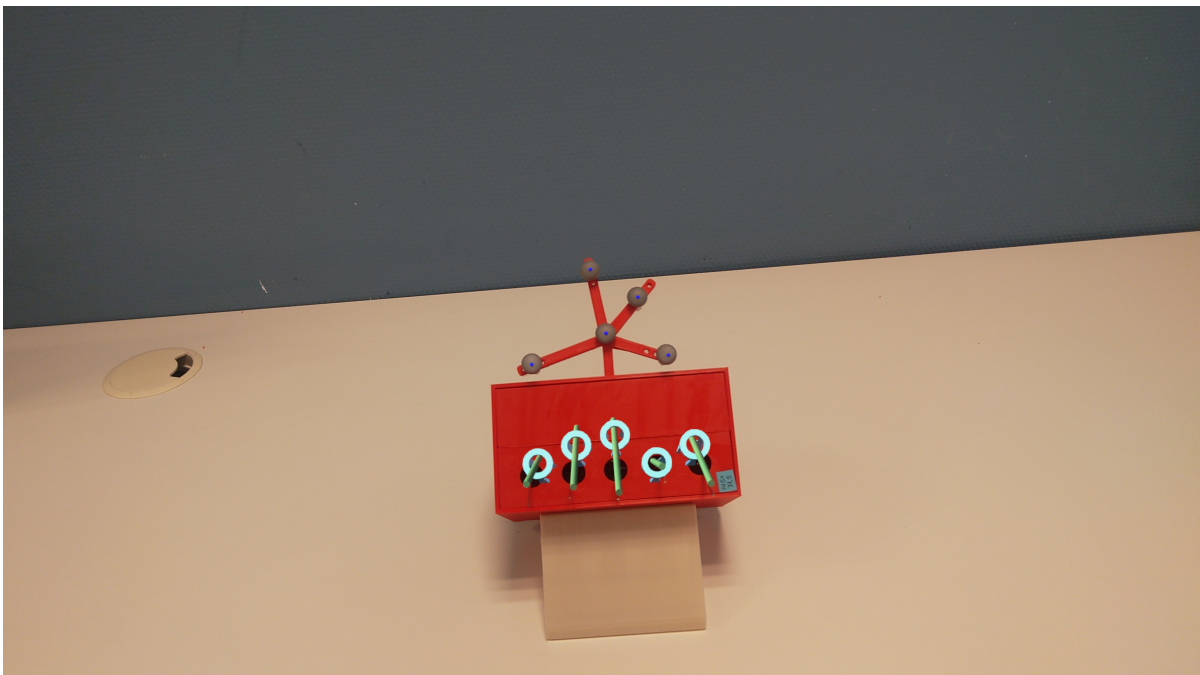


Figure 27: The holographic rings (light blue) and planned K-wires (green) are superimposed on the phantom. The center points of each IR marker are shown in blue.

4.2.4 K-wires placement

With this overlay as guidance, the participant will then insert the K-wires according to the planning. The participant gets one try for each K-wire and must stop when the K-wire hits the ring or the back of the phantom. This is to ensure the K-wire is placed with only AR as guidance and not because of any haptic feedback. Figure 28 shows a participant inserting K-wires into the phantom with the guidance of AR. In total, five participants performed the experiment. One participant executed the experiment three times. This was to investigate the learning curve.

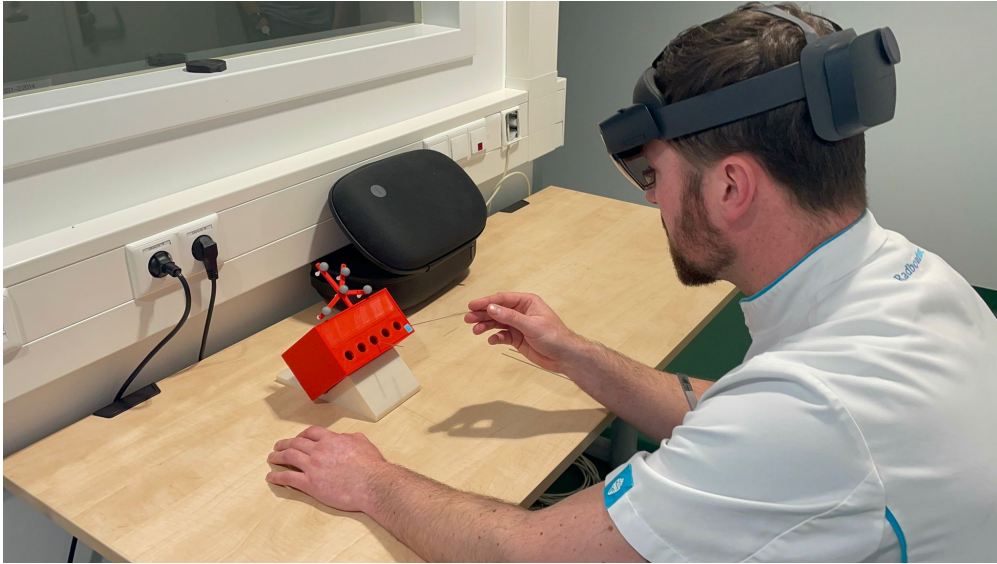


Figure 28: The participant uses AR as guidance for inserting K-wires

4.2.5 CBCT scanner

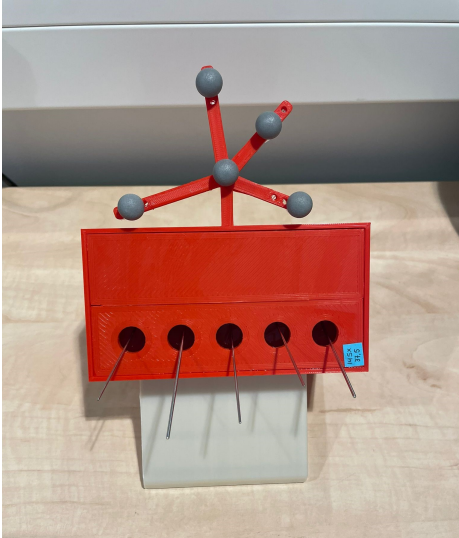
After placing the K-wires, a CBCT scan of the phantom was made. The phantom was positioned at an angle for scanning as can be seen in figure 29.



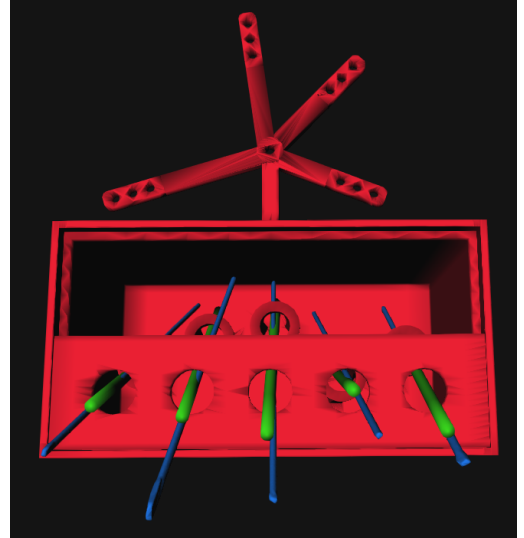
Figure 29: Phantom in the CBCT scanner

4.2.6 Segmentation

From the DICOM files a segmentation was made using Mimics. The phantom and the five K-wires were segmented separately and saved as STL files. These STL files were then loaded in 3DMedX along with the designed phantom and the corresponding planning. With the Procrustes algorithm, the 3D reconstructed phantom was matched with the designed phantom. The same transformation matrix was then used for the 3D reconstructed K-wires. Figure 30 shows the physical phantom (a) and its 3D reconstructed version (b) with inserted K-wires in blue, planned K-wires in green and the designed phantom in red. The 3D reconstruction of each participant can be found in Appendix C.



(a) Phantom after the K-wires insertion



(b) 3D reconstruction of the designed phantom (red) with inserted K-wires (blue) and the planned K-wires (green)

Figure 30: Phantom with inserted K-wires in the real world (a) and the virtual world (b)

4.2.7 Measurements

For each placed K-wire four measurements were performed. The first measurement is whether the K-wire goes through the ring or not indicated with hit or no hit. The second measurement is the Euclidean distance of the entry point between the planned and inserted K-wire as is presented with E in figure 31. The entry point was defined at 9.5 cm height, because of the 0.5 cm thickness of the lid. The third measurement is the Euclidean distance of the endpoint between the planned and inserted K-wire defined as F. The reference length of a sacroiliac screw for the S1 is around 15 cm.[42] However, due to the phantom's small size which was limited by the scan volume, it was decided to use a length half as short. The K-wire's length at 7.5 cm was set as the endpoint. The last measurement is the angle between the planned and inserted K-wire, shown in figure 31 as G.

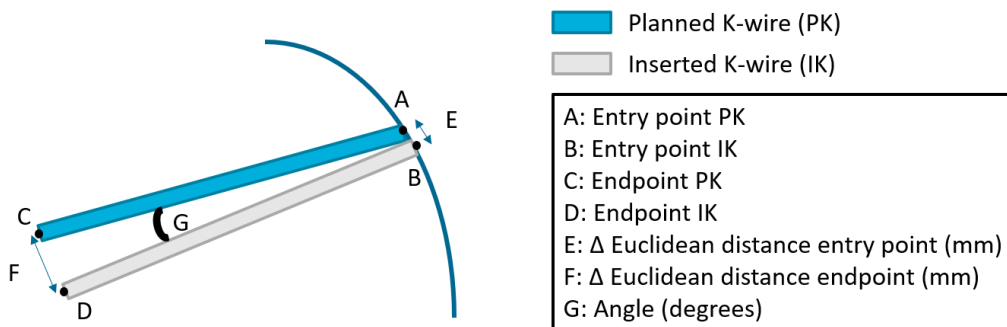


Figure 31: Overview of the analyses depicted as the Euclidean distance of entry point (E) and endpoint (F) between the planned and inserted K-wire. The angle between the planned and inserted K-wire is depicted with G.

4.3 Results

In table 3 an overview of the first measurement is shown. It describes whether a K-wire went through the ring indicated with a hit. No hit means that the K-wire went outside or against the ring. Table 3 shows the results per participant. The positioning of the rings was counted from left to right where the ring positioned on the most left side was called position 1. In total, 69% of the inserted K-wires were hits and 31% were no hits as illustrated in figure 32.

Table 3: Overview of hit/no hit per test for each ring. Hit describes the K-wires that passed through the rings. No hit describes the K-wires outside the rings.

Hit/No hit	Position1	Position2	Position3	Position4	Position5
Test1	No hit	No hit	Hit	No hit	Hit
Test2	Hit	Hit	Hit	Hit	Hit
Test3	Hit	Hit	Hit	No hit	Hit
Test4	Hit	Hit	Hit	No hit	Hit
Test5	No hit	Hit	No hit	Hit	No hit
Test6	Hit	Hit	No hit	No hit	Hit
Test7	Hit	Hit	Hit	No hit	Hit

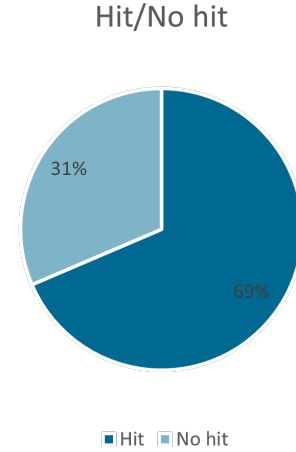


Figure 32: Percentage hit/no hit of all participants combined

Table 4 presents the second measurement: Euclidean distance of the entry point between inserted and planned K-wires. The results of each participant for the five positions are illustrated. The median, mean, minimum and maximum values for each position are presented in a graph (figure 33). The mean of all positions and tests together is 2.57 mm. The highest error is in position 3 with a mean error of 3.58 mm and a maximum error of 6.05 mm.

Table 4: Δ Euclidean distances (mm) of the entry point between planned and inserted K-wires for each test and each position. The mean was calculated for each test.

Δ Entry point (mm)	Position1	Position2	Position3	Position4	Position5	Mean
Test1	0.89	0.85	4.56	2.00	2.82	2.22
Test2	1.88	2.87	3.92	1.49	2.61	2.55
Test3	1.96	2.16	1.83	3.34	1.90	2.24
Test4	2.64	0.73	0.23	2.30	1.83	1.55
Test5	3.61	4.93	5.96	0.31	1.76	3.32
Test6	2.86	3.59	6.05	2.17	2.01	3.34
Test7	3.27	3.67	2.47	2.44	2.13	2.80

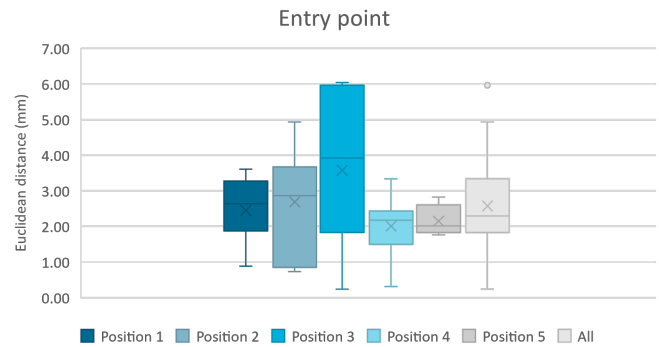


Figure 33: The box plot displays the median (-), mean (x), minimum and maximum values, and outliers (o) for each position and at the entry point

Table 5 presents the third measurement: euclidean distance of the endpoint between inserted and planned K-wires. The results of each participant for the five positions are illustrated. The median, mean, minimum and maximum values for each position are presented in a graph (figure 34). Only the data from K-wires that went through the rings are shown. The mean of all positions and tests together is 4.71 mm. The maximum error is 7.73 mm in position 5. When the data of the no hits are included, the mean error is 8.06 mm and the maximum error is 20.34 mm.

Table 5: Euclidean distances (mm) of the endpoint between planned and inserted K-wires for each test and each position that went through the ring (hit). The mean was calculated for each test.

Δ Endpoint (mm)	Position1	Position2	Position3	Position4	Position5	Mean
Test1	-	-	4.82	-	5.66	5.24
Test2	5.97	6.17	4.14	6.21	5.81	5.66
Test3	5.63	2.55	2.08	-	4.63	3.72
Test4	5.08	3.70	0.72	-	5.69	3.80
Test5	-	5.67	-	6.56	-	6.12
Test6	4.82	4.57	-	-	7.73	5.71
Test7	4.93	4.53	0.91	-	4.35	3.68

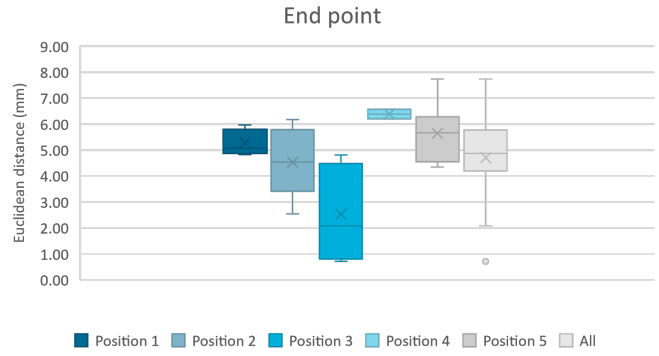


Figure 34: The box plot displays the median (-), mean (x), minimum and maximum values, and outliers (o) for each position and at the endpoint

Table 6 presents the last measurement: angle in degrees between inserted and planned K-wires. The results of each participant for the five positions are illustrated. The median, mean, minimum and maximum values for each position are presented in a graph (figure 35). Only the K-wires that went through the ring are included in this graph. The angles of the missing hits were often large and seen as outliers. The mean of all positions and tests together is 4.68° with a maximum error of 7.21° . When the data of the no hits are included, the mean error is 7.02° and the maximum error is 16.32° .

Table 6: Angle in degrees between planned and inserted K-wires for each test subject and each position. The mean was calculated for each test.

Angle($^\circ$)	Position1	Position2	Position3	Position4	Position5	Mean
Test1	13.84	12.99	6.17	15.35	6.19	10.91
Test2	5.86	6.35	5.33	3.70	6.16	5.48
Test3	5.60	0.40	2.53	10.61	4.49	4.73
Test4	5.34	2.90	0.59	3.85	3.28	3.20
Test5	5.27	7.21	12.82	5.04	13.07	8.68
Test6	5.65	5.55	15.57	16.32	6.64	9.94
Test7	5.51	5.68	2.35	13.75	3.91	6.24

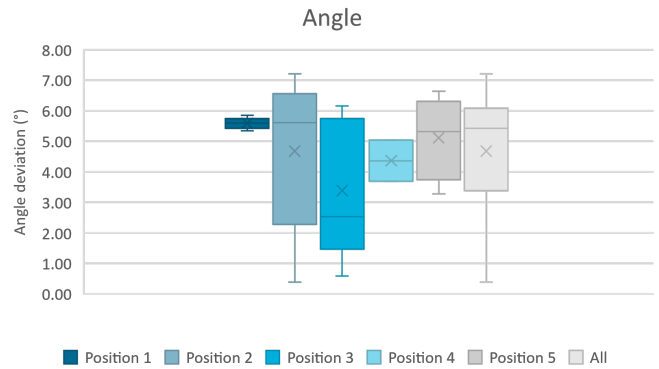


Figure 35: The box plot displays the median (-), mean (x), minimum and maximum angles for each position that was a hit.

Figure 36 shows the learning curve of participant 5 (test5, test6 and test7). It can be seen that the number of hits increases after each time. The mean errors of entry point, endpoint and angle are all smaller the third time compared to the first attempt.

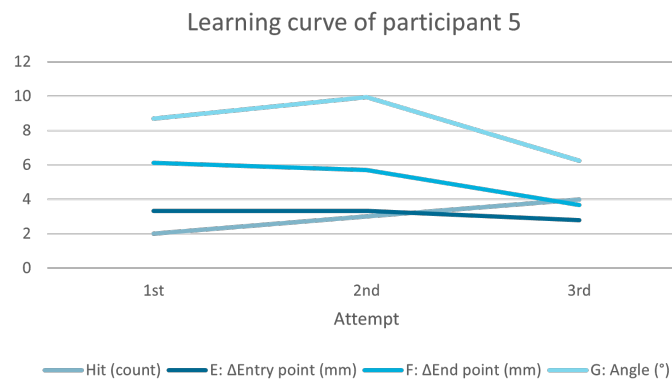


Figure 36: Learning curve of participant 5

4.4 Discussion

4.4.1 Interpretation of the results

In figure 32 it can be seen that around 70% of the K-wires went through the ring successfully. It can be noticed in table 3 that position 4 was the hardest to place the K-wire through the ring. Only two out of seven times was the K-wire placed correctly. This can be clarified by the position of the ring. The opening of the ring is parallel to the opening of the lid, creating a pathway that is perpendicular. This pathway was hard to follow because the direction of the planning was difficult to see.

From the results, it is noticeable that the combination of the entry point and angle influences the endpoint. When both the entry point and the angle have a small error, the error of the endpoint will also be small. This can be seen in test4 position 3 where the entry point is 0.23 mm and the angle 0.59°, resulting in an endpoint error of 0.72 mm. Another observation that can be made, is that almost all K-wires that did not go through the rings had a high angle deviation. Even if the entry point had a small error (Test1, position 1 and 2), the angle deviation was too large which ended in a no-hit.

Looking at the results for each test, it can be noticed that the mean error of the Δ Entry point (E) ranges from 1.55 to 3.34 mm. This deviation is smaller than that of the Δ Endpoint (F) and Angle (G), where the ranges are from 3.68 to 6.12 mm and from 3.20 to 10.91° respectively. Of which the calculated mean errors of the endpoint are without the no hits. This inconsistency between each test can be clarified by the lack of feedback during the insertion of the K-wire. The assessment is easier to make at the entry point because the K-wire can still be seen and compared to the planning. This is not the same for the endpoint and the angle. When the K-wire enters the phantom, visuals of the tip's K-wire are lost and only the end of the K-wire is visible. Therefore, making the assessment on how to steer the K-wire difficult.

Test5 through test7 were executed by the same participant. Figure 36 shows the learning curve of this participant. It can be seen that the third attempt has more hits and smaller errors for the entry point, endpoint and angle. It seems that practicing may improve the outcome. However, more participants should be tested multiple times before a conclusion can be made about the learning curve.

The mean error was 2.57 mm for the entry point and 4.71 mm for the endpoint. Both values exceed the limit of 2 mm which is needed for accurate percutaneous screw fixation in the pelvis. Additionally, only 69% of the K-wires were positioned within the rings. Further research and optimization of the application is needed before it can be used clinically. The accuracy should be improved and a better precision should be achieved.

4.4.2 Limitations

During the experiment, several observations were made. First, the lack of feedback while inserting the K-wire. As mentioned before, it was difficult to assess how to steer the K-wire, because the tip of the K-wire was not visible after entering the phantom. This makes the procedure very subjective. A promising solution for this problem could be tool tracking. If the K-wire could be tracked, then the pathway of the K-wire could be calculated and compared with the planning. A feedback system could be made where the AR application shows the user how to move and position the K-wire in order to place it correctly. This may also decrease the cognitive load for the user.[23] Second, at the time of creating the phantom, it was assumed that the K-wires remained its position after insertion. However, during the experiment, sometimes it occurred that the K-wire collided with the ring. Preventing the K-wire from moving further into the phantom. The weight of the K-wire that was not inserted into the phantom was sometimes too heavy, making the gelatin rupture and causing some displacement of the K-wire. Further research on different materials that may replace gelatin should be considered. On top of that, these K-wires were not included in the endpoint measurement, because they did not reach the 7.5 cm. However, these K-wires are important to measure, because they are also the ones that have the highest errors. Other targets than rings or a different phantom should be used. Lastly, some participants said that the hologram was a bit blurred or did not match with the phantom. Each participant has

a different eyesight and may view the hologram differently. Doing eye calibration for each participant may solve the problem. Looking through the camera on a screen at the same time as the participant may help in understanding the problem better. However, accessing multiple cameras at the same time during research mode is not possible. Taking a questionnaire at the end of the experiment may also give additional information about the participant's experience.

There were a few limitations of the materials. The K-wires that were used during the experiment, were collected at the OR where they have been used during surgery. There is a possibility that the K-wires were slightly bent. This may have some effect on the analyses. For future experiments, it is recommended to use K-wires that have not been used before. This prevents possible inaccuracies in the results. Another limitation was the gelatin that was used to fill the phantom. The original plan was to replace the gelatin after each experiment, because the K-wire causes damage to the gelatin and may form a pathway in the gelatin. However, this was very time consuming and cost a lot of gelatin. On top of that, no difference was felt after inserting the K-wires multiple times into the phantom. The only risk was that the K-wires were less fixed. After these considerations, a decision was made to reuse the phantom. The phantoms were used a maximum of six times and an additional CBCT scan was made. Some air in the gelatin was visible on these scans. To prevent this problem, the phantom should be replaced after each experiment, other materials need to be used or the phantom should be redesigned as discussed before.

The proof of concept was tested in this experiment. A simplification of the clinical procedure was performed. The next step should be performing the experiment in a more clinical setting. The K-wires were now inserted by hand, but performing this with a drill should also be tested. This is more in line with reality. On top of that, a new design of the phantom that is more similar to the anatomy of the bony pelvis or even a cadaver should be used. Lastly, the experiment could be executed in the OR and a simulation of the percutaneous screw fixation of the pelvis with AR could be done.

4.5 Conclusion

In this chapter, an experiment was executed where the participants needed to insert K-wires through rings with augmented reality as guidance. Analyses were made by comparing the inserted K-wires with the planning. The accuracy was not under the limit of 2 mm. Adding tool tracking to the AR application may increase the accuracy of the performance. Further research needs to be done to upgrade the experiment and bring it closer to a clinical setting.

5 General discussion and conclusion

The primary aim of this thesis was to develop an augmented reality application that can detect IR markers (Chapter 3) and be used as a surgical navigation tool. The results look very promising as the accuracy is under the limit of 2 mm.

Chapter 2 showed the design and 3D-printing process of the reference star and the phantom. IR markers could be attached to the reference star and the phantom. Virtual and physical measurements were made and compared to the design. The print error could be neglected, because of the small errors.

The second aim was to investigate the accuracy of the developed augmented reality application while performing a simulation of the clinical procedure. An experiment (Chapter 4) was successfully executed where a simplification of the percutaneous screw fixation of the pelvis was simulated. K-wires were inserted into the phantom with the guidance of the AR application. A comparison between the inserted and planned K-wires was made. Analyses of the insertion, entry point, endpoint and angle deviation were performed. For clinical relevance, it is important that the accuracy of K-wire placement is within the range of 2 mm. This is to prevent neurovascular damage.[20] From the results of the experiment, the accuracy of 2 mm is not yet achieved.

Further research is needed to improve the accuracy of the AR application. This can be done by improving the segmentation, registration and calibration of the AR application. On top of that, adding tool tracking to the AR application should also increase the accuracy. Tool tracking could give feedback to the participant during the procedure, so the participant will have more information about how to steer the K-wire to its correct position. Furthermore, improvement of the experiment should be done by bringing it closer to a clinical setting. This can be achieved by using more anatomically realistic phantoms or even cadavers. The experiment should also be executed more like the real procedure of the percutaneous screw fixation of the pelvis and using the right instruments.

Before augmented reality can be implemented in the clinic, more research is needed. However, when the right accuracy and precision are achieved, the impact of this kind of surgical navigation technique can be big. Every procedure that could have added value by superimposing information on the patient may benefit from this technique. This can range from screw fixation, and needle insertion, to tumor localization.[26] The benefits of this surgical navigation technique is that it eliminates the "switching focus" problem and decreases the cognitive load of the surgeon. This could lead to better focus of the surgeon and fewer errors.

The research presented in this thesis provides a proof of concept for performing percutaneous screw fixation of the pelvis using augmented reality with IR marker tracking as guidance. Further improvement of the augmented reality application is needed before it can be implemented clinically.

References

- [1] M. Burgess and F. Lui, *Anatomy, Bony Pelvis and Lower Limb: Pelvic Bones*. StatPearls Publishing, 2022.
- [2] K. Perry, A. Mabrouk, and B. Chauvin, *Pelvic Ring Injuries*. StatPearls Publishing, 2022.
- [3] H. Bakker, M. Tijsterman, B. Kubat, V. Soerdjbalie-Maikoe, R. Rijn, and B. de Bakker, “Postmortem radiological case series of acetabular fractures after fatal aviation accidents,” *Forensic Science, Medicine and Pathology*, vol. 14, Mar. 2018. DOI: 10.1007/s12024-018-9946-1.
- [4] O. Hauschild, P. C. Strohm, U. Culemann, *et al.*, “Mortality in Patients With Pelvic Fractures: Results From the German Pelvic Injury Register,” *Journal of Trauma and Acute Care Surgery*, vol. 64, no. 2, 2008, ISSN: 2163-0755. [Online]. Available: https://journals.lww.com/jtrauma/Fulltext/2008/02000/Mortality_in_Patients_With_Pelvic_Fractures_.31.aspx.
- [5] L. Flint and H. G. Cryer, “Pelvic Fracture: The Last 50 Years,” *Journal of Trauma and Acute Care Surgery*, vol. 69, no. 3, 2010, ISSN: 2163-0755. [Online]. Available: https://journals.lww.com/jtrauma/Fulltext/2010/09000/Pelvic_Fracture__The_Last_50_Years.1.aspx.
- [6] J.-P. Chen, P.-J. Tsai, C.-Y. Su, *et al.*, “Percutaneous iliosacral screw and trans-iliac trans-sacral screw with single C-arm fluoroscope intensifier is a safe treatment for pelvic ring injuries,” *Scientific Reports*, vol. 12, no. 1, p. 368, 2022, ISSN: 2045-2322. DOI: 10.1038/s41598-021-04351-z. [Online]. Available: <https://doi.org/10.1038/s41598-021-04351-z>.
- [7] T. Pohlemann, A. Gänsslen, O. Schellwald, U. Culemann, and H. Tscherne, “Outcome after pelvic ring injuries,” *Injury*, vol. 27, pp. 31–38, 1996, ISSN: 00201383. DOI: 10.1016/S0002-9378(15)33150-1.
- [8] D. Davis, L. Foris, S. Kane, and M. Waseem, *Pelvic Fracture*. StatPearls Publishing, 2022.
- [9] T. B. Alton and A. O. Gee, “Classifications in Brief: Young and Burgess Classification of Pelvic Ring Injuries,” *Clinical Orthopaedics & Related Research*, vol. 472, no. 8, pp. 2338–2342, Aug. 2014, ISSN: 0009-921X. DOI: 10.1007/s11999-014-3693-8.
- [10] M. J. Halawi, “Pelvic ring injuries: Surgical management and long-term outcomes,” *Journal of Clinical Orthopaedics and Trauma*, vol. 7, no. 1, pp. 1–6, Jan. 2016, ISSN: 09765662. DOI: 10.1016/j.jcot.2015.08.001.
- [11] H. Caviglia, A. Mejail, M. E. Landro, and N. Vatani, “Percutaneous fixation of acetabular fractures,” *EFORT Open Reviews*, vol. 3, no. 5, pp. 326–334, May 2018, ISSN: 2396-7544. DOI: 10.1302/2058-5241.3.170054.
- [12] D. Höntzsch, *AO Surgery Reference: External fixation*. [Online]. Available: <https://surgeryreference.aofoundation.org/orthopedic-trauma/adult-trauma/pelvic-ring/basic-technique/external-fixation#pin-insertion-in-supra-acetabular-position>.
- [13] R. Banerjee, P. Brink, M. Cimerman, T. Pohlemann, and M. Tomazevic, *AO Surgery Reference: ORIF - Pubic ramus plate*. [Online]. Available: <https://surgeryreference.aofoundation.org/orthopedic-trauma/adult-trauma/pelvic-ring/intact-posterior-arch-uni-or-bilateral-fracture-anterior-arch/orif-pubic-ramus-plate>.
- [14] R. Banerjee, P. Brink, M. Cimerman, T. Pohlemann, and M. Tomazevic, *AO Surgery Reference: Operative treatment*. [Online]. Available: <https://surgeryreference.aofoundation.org/orthopedic-trauma/adult-trauma/pelvic-ring/incomplete-disruption-posterior-arch-lateral-compression-fracture/operative-treatment#reduction-and-fixation>.
- [15] H. A. Cruz and G. P. d. Angelis, “Sacroiliac secure corridor: analysis for safe insertion of iliosacral screws,” *Revista Brasileira de Ortopedia (English Edition)*, vol. 48, no. 4, pp. 348–356, Jul. 2013, ISSN: 22554971. DOI: 10.1016/j.rboe.2013.04.006.
- [16] D. Wagner, L. Kamer, T. Sawaguchi, *et al.*, “Critical dimensions of trans-sacral corridors assessed by 3D CT models: Relevance for implant positioning in fractures of the sacrum,” *Journal of Orthopaedic Research*, vol. 35, no. 11, pp. 2577–2584, Nov. 2017, ISSN: 07360266. DOI: 10.1002/jor.23554.

- [17] C. M. Andrews, A. B. Henry, I. M. Soriano, M. K. Southworth, and J. R. Silva, "Registration Techniques for Clinical Applications of Three-Dimensional Augmented Reality Devices," *IEEE journal of translational engineering in health and medicine*, vol. 9, p. 4900214, 2021, ISSN: 2168-2372. DOI: 10.1109/JTEHM.2020.3045642.
- [18] P. H. Richter, F. Gebhard, C. Dehner, and A. Scola, "Accuracy of computer-assisted iliosacral screw placement using a hybrid operating room," *Injury*, vol. 47, no. 2, pp. 402–407, 2016, ISSN: 0020-1383. DOI: <https://doi.org/10.1016/j.injury.2015.11.023>. [Online]. Available: <https://www.sciencedirect.com/science/article/pii/S0020138315007457>.
- [19] M. Kułakowski, P. Reichert, K. Elster, *et al.*, "Differences in Accuracy and Radiation Dose in Placement of Iliosacral Screws: Comparison between 3D and 2D Fluoroscopy," *Journal of Clinical Medicine*, vol. 11, no. 6, p. 1466, Mar. 2022, ISSN: 2077-0383. DOI: 10.3390/jcm11061466.
- [20] R. Hartensuer, M. F. Lodde, J. Keller, *et al.*, "Safety, Effect and Feasibility of Percutaneous SI-Screw with and without Augmentation—A 15-Year Retrospective Analysis on over 640 Screws," *Journal of Clinical Medicine*, vol. 9, no. 8, 2020, ISSN: 2077-0383. DOI: 10.3390/jcm9082660. [Online]. Available: <https://www.mdpi.com/2077-0383/9/8/2660>.
- [21] A. Q. A. Teo, J. H. Yik, S. N. Jin Keat, D. P. Murphy, and G. K. O'Neill, "Accuracy of sacroiliac screw placement with and without intraoperative navigation and clinical application of the sacral dysmorphism score," *Injury*, vol. 49, no. 7, pp. 1302–1306, Jul. 2018, ISSN: 00201383. DOI: 10.1016/j.injury.2018.05.027.
- [22] J.-S. Jarvers, S. Katscher, A. Franck, *et al.*, "3D-based navigation in posterior stabilisations of the cervical and thoracic spine: problems and benefits. Results of 451 screws," *European Journal of Trauma and Emergency Surgery*, vol. 37, no. 2, pp. 109–119, 2011, ISSN: 1863-9941. DOI: 10.1007/s00068-011-0098-1. [Online]. Available: <https://doi.org/10.1007/s00068-011-0098-1>.
- [23] M. Herrlich, P. Tavakol, D. Black, *et al.*, "Instrument-mounted displays for reducing cognitive load during surgical navigation," *International Journal of Computer Assisted Radiology and Surgery*, vol. 12, no. 9, pp. 1599–1605, 2017, ISSN: 1861-6429. DOI: 10.1007/s11548-017-1540-6. [Online]. Available: <https://doi.org/10.1007/s11548-017-1540-6>.
- [24] B. J. Park, S. J. Hunt, G. J. Nadolski, and T. P. Gade, "Augmented reality improves procedural efficiency and reduces radiation dose for CT-guided lesion targeting: a phantom study using HoloLens 2," *Scientific Reports*, vol. 10, no. 1, p. 18620, Oct. 2020, ISSN: 2045-2322. DOI: 10.1038/s41598-020-75676-4.
- [25] A. W. K. Yeung, A. Tosevska, E. Klager, *et al.*, "Virtual and Augmented Reality Applications in Medicine: Analysis of the Scientific Literature," *Journal of Medical Internet Research*, vol. 23, no. 2, e25499, Feb. 2021, ISSN: 1438-8871. DOI: 10.2196/25499.
- [26] S. Malhotra, O. Halabi, S. P. Dakua, J. Padhan, S. Paul, and W. Palliyali, "Augmented Reality in Surgical Navigation: A Review of Evaluation and Validation Metrics," *Applied Sciences*, vol. 13, no. 3, p. 1629, Jan. 2023, ISSN: 2076-3417. DOI: 10.3390/app13031629.
- [27] C. Kunz, P. Maurer, F. Kees, *et al.*, "Infrared marker tracking with the HoloLens for neurosurgical interventions," *Current Directions in Biomedical Engineering*, vol. 6, no. 1, 2020. DOI: doi:10.1515/cdbme-2020-0027. [Online]. Available: <https://doi.org/10.1515/cdbme-2020-0027>.
- [28] K.-T. Huang, C. Ball, J. Francis, R. Ratan, J. Boumis, and J. Fordham, "Augmented Versus Virtual Reality in Education: An Exploratory Study Examining Science Knowledge Retention When Using Augmented Reality/Virtual Reality Mobile Applications," *Cyberpsychology, Behavior, and Social Networking*, vol. 22, no. 2, pp. 105–110, Jan. 2019, ISSN: 2152-2715. DOI: 10.1089/cyber.2018.0150. [Online]. Available: <https://doi.org/10.1089/cyber.2018.0150>.
- [29] *About HoloLens 2*, Mar. 2023. [Online]. Available: <https://learn.microsoft.com/en-us/hololens/hololens2-hardware>.

- [30] D. Niedermayr and J. Wolfartsberger, "Analyzing the potential of a time-of-flight depth sensor for assembly assistance," *Procedia Computer Science*, vol. 200, pp. 648–659, 2022, ISSN: 1877-0509. DOI: <https://doi.org/10.1016/j.procs.2022.01.263>. [Online]. Available: <https://www.sciencedirect.com/science/article/pii/S1877050922002721>.
- [31] P. Hübner, K. Clintworth, Q. Liu, M. Weinmann, and S. Wursthorn, "Evaluation of HoloLens Tracking and Depth Sensing for Indoor Mapping Applications," *Sensors*, vol. 20, no. 4, p. 1021, Feb. 2020, ISSN: 1424-8220. DOI: 10.3390/s20041021.
- [32] *HoloLens Research Mode*, Apr. 2022. [Online]. Available: <https://learn.microsoft.com/en-us/windows/mixed-reality/develop/advanced-concepts/research-mode#enabling-research-mode-hololens-1st-gen-and-hololens-2>.
- [33] A. Cao, A. Dhanaliwala, J. Shi, T. Gade, and B. Park, "Image-based marker tracking and registration for intraoperative 3D image-guided interventions using augmented reality," in *Medical Imaging 2020: Imaging Informatics for Healthcare, Research, and Applications*, T. M. Deserno and P.-H. Chen, Eds., SPIE, Mar. 2020, p. 1, ISBN: 9781510634039. DOI: 10.1117/12.2550415.
- [34] J. W. Meulstee, J. Nijsink, R. Schreurs, *et al.*, "Toward Holographic-Guided Surgery," *Surgical Innovation*, vol. 26, no. 1, pp. 86–94, Sep. 2018, ISSN: 1553-3506. DOI: 10.1177/1553350618799552. [Online]. Available: <https://doi.org/10.1177/1553350618799552>.
- [35] J. Shin, R. S. Sandhu, and G. Shih, "Imaging Properties of 3D Printed Materials: Multi-Energy CT of Filament Polymers," *Journal of Digital Imaging*, vol. 30, no. 5, pp. 572–575, Oct. 2017, ISSN: 0897-1889. DOI: 10.1007/s10278-017-9954-9.
- [36] J. Suder, Z. Bobovsky, J. Mlotek, M. Vocetka, Z. Zeman, and M. Safar, "EXPERIMENTAL ANALYSIS OF TEMPERATURE RESISTANCE OF 3D PRINTED PLA COMPONENTS," *MM Science Journal*, vol. 2021, no. 1, pp. 4322–4327, Mar. 2021, ISSN: 18031269. DOI: 10.17973/MMSJ.2021{_}03{_}2021004.
- [37] J. Bouwmeester, "Manuscript anthropomorphic model pelvis," Ph.D. dissertation, University of Twente, 2022.
- [38] Petergu684, HoloAdventure, and vbandi, *HoloLens2-ResearchMode-Urinity*, 2020.
- [39] R. Muthukrishnan, "Edge Detection Techniques For Image Segmentation," *International journal of computer science and information technology*, vol. 3, pp. 259–267, Dec. 2011. DOI: 10.5121/ijcsit.
- [40] JavaTpoint, *Brute force approach*. [Online]. Available: <https://www.javatpoint.com/brute-force-approach>.
- [41] F. Van Der Heijden, "SNT 1 - Point Registration," 2020.
- [42] Y. Zhao, J. Li, D. Wang, and W. Lian, "Parameters of lengthened sacroiliac screw fixation: a radiological anatomy study," *European Spine Journal*, vol. 21, no. 9, pp. 1807–1814, Sep. 2012, ISSN: 0940-6719. DOI: 10.1007/s00586-012-2367-z.

Appendix

A Failed 3D prints



Figure 37: Failed 3D print with PLA and PVA in the 3D printer

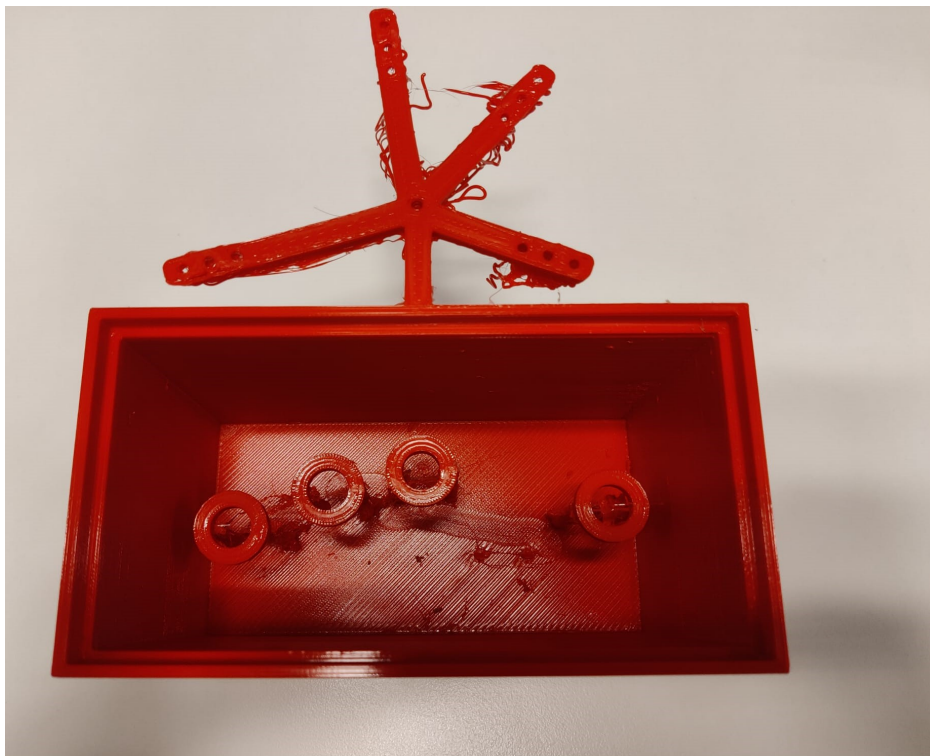


Figure 38: Failed 3D print with PLA and PVA, after removing support

B Segmentation with scattering

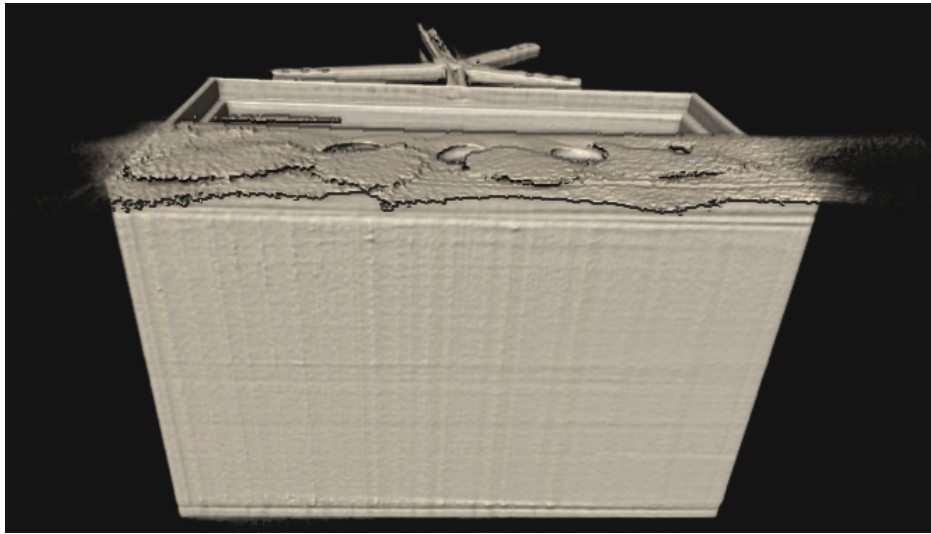
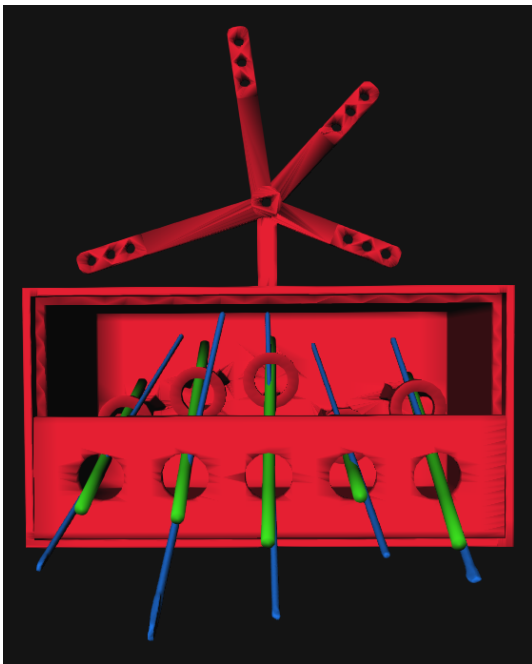
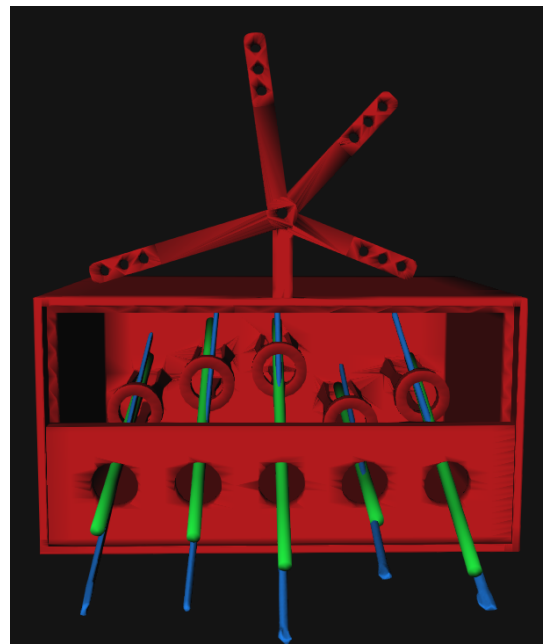


Figure 39: Segmentation of phantom 8 with scattering at the top.

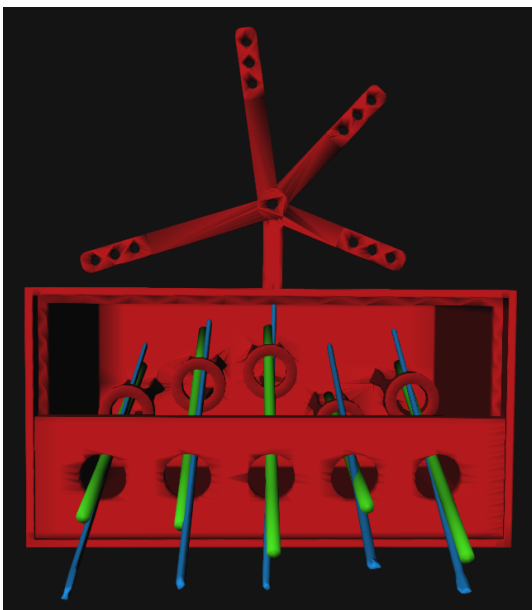
C 3D reconstructions of the placed K-wires



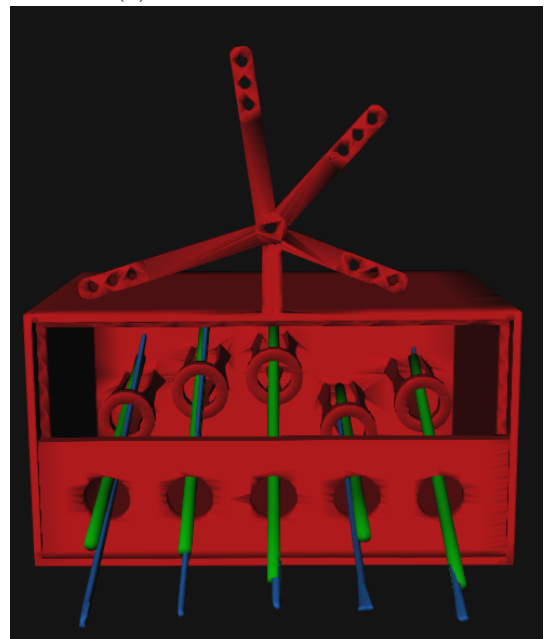
(a) 3D reconstruction of test1



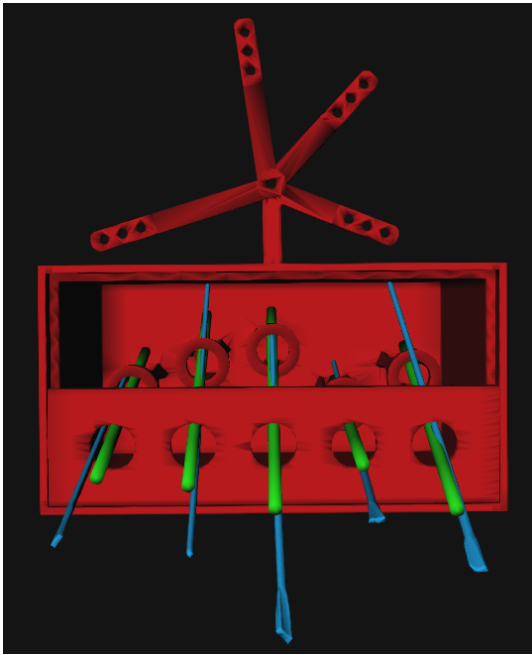
(b) 3D reconstruction of test2



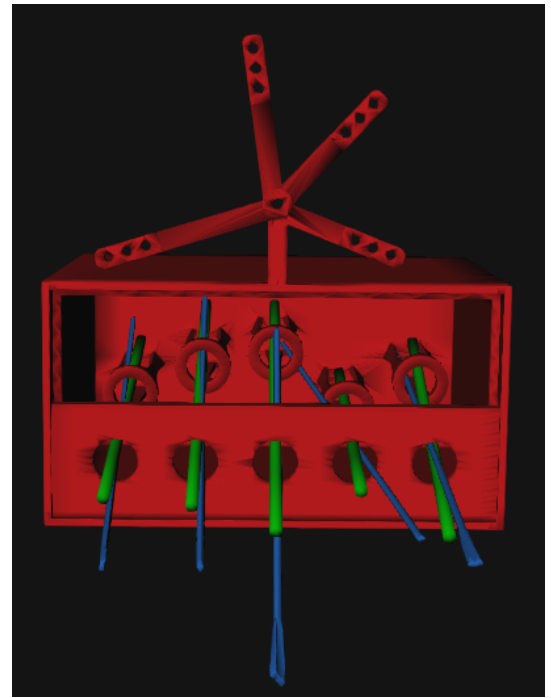
(c) 3D reconstruction of test3



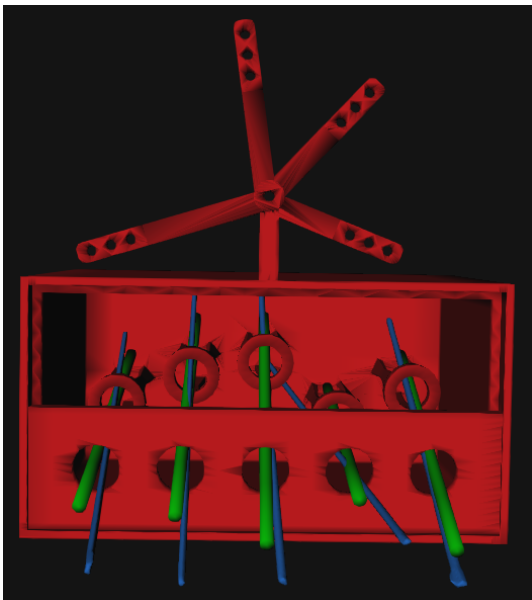
(d) 3D reconstruction of test4



(e) 3D reconstruction of test5



(f) 3D reconstruction of test6



(g) 3D reconstruction of test7

Figure 40: 3D reconstructions of all tests. Phantom in red, planned K-wires in green and placed K-wires in blue.